Sergi Cervilla García

Comparison of spatial transcriptomics technologies across six cancer types

MASTER'S THESIS

supervised by Dr. Eduard Porta Pardo

Master's Degree in Biomedical Data Science

Barcelona, 2024

Dr. Eduard Porta Pardo, certifies that the student Sergi Cervilla García has elaborated the work under his direction and he authorizes the presentation of this Master's Thesis for its evaluation.

Advisor signature:

Acknowledgements

First and foremost, I would like to express my immense gratitude to all the people who supported me during the lengthy process of my master's thesis project. Starting from my family and close friends who gave endless support. Followed by Cancer Immunogenomics group in the Josep Carreras Leukaemia Research Institute who welcomed me into their group, and I had valuable insights from the numerous discussions about the project. Special thanks go to Daniela Grases for her exceptional work in the wet lab with the samples I analyzed, and to Eduard Porta for his continuous supervision, guidance, and significant advice throughout the entire process. Finally, to thank Asociación Española Contra el Cáncer who supported me (LABAE20038PORT)

This work was supported by Nanostring and Longwood Laboratories (who funded the CosMx experiments), 10x Genomics and Bonsai Labs (who funded the Xenium experiments), and AECC (who funded the VISIUM experiments, LABAE20038PORT).

List of contents

List of Figures

Abstract

Spatial biology experiments integrate the molecular and histological landscape of tissues to provide a previously inaccessible view of tissue biology, unlocking the architecture of complex multicellular tissues. Within spatial biology, spatial transcriptomics platforms are among the most advanced, allowing researchers to characterize the expression of thousands of genes across space. These new technologies are transforming our understanding of how cells are organized in space and communicate with each other to determine emergent phenotypes with unprecedented granularity. This is particularly important in cancer research, as it is becoming evident that tumor evolution is shaped not only by the genetic properties of cancer cells but also by how they interact with the tumor microenvironment and their spatial organization. While many platforms can generate spatial transcriptomics profiles, it is still unclear in which context each platform better suits the needs of its users. Here we compare the results obtained using 4 different spatial transcriptomics (VISIUM, VISIUM CytAssist, Xenium and CosMx) and one spatial proteomics (VISIUM CytAssist) platforms across serial sections of 6 FFPE samples from primary human tumors covering some of the most common forms of the disease (lung, breast, colorectal, bladder, lymphoma and ovary). We observed that the VISIUM platform with CytAssist chemistry yielded superior data quality. Xenium consistently produced more reliable results for *in situ* platforms, with better gene clustering and fewer false positives than CosMx. Interestingly, these platform-based variations didn't significantly affect cell type identification. Finally, by comparing VISIUM protein profiles with the spatial transcriptomics data from all four platforms on each sample, we identified several genes with mismatched RNA and protein expression patterns, highlighting the importance of multi-omics profiling to reveal the true biology of human tumors.

1. Introduction

1.1 Importance of Spatial Transcriptomics

The understanding of complex systems, such as tumors, has been widely explored using different angles and approaches to understand the wide range of information layers that they contain[1–4]. Among them, we can find the identification of mutations (genomics)[5], the quantification of gene (transcriptomics)[6] and protein (proteomics)[7] expression and the measurement of metabolites abundance (metabolomics)[8]. In particular, transcriptomics has been deeply explored in the last decades since it allows researchers to capture the real-time activities of cells by measuring gene activity. This is particularly important in understanding how cells respond to various stimuli, how they differentiate, and how they interact within their microenvironment which is important in the study of cancer. The transcriptomics field has evolved during the past years thanks to the developments of next-sequencing (NGS) approaches[9]. Within the transcriptomics era, we can distinguish three main stages[10].

In the beginning, we had Bulk-RNA where the expression is captured by averaging the gene expression of the cells in a sample[11,12]. The generation of this data is cost-efficient and scalable, allowing researchers to decipher important insights such as over- or down-expression of genes in cancer cells compared to normal cells. Examples of its usefulness in a large cohort can be observed in The Cancer Genome Atlas[13]. However, Bulk-RNA sequencing had limitations, as the diversity of cell types and states within a sample could mask the transcriptomic profiles. The intermixed signals could ignore the contributions of rare cell types and fail to capture the heterogeneity within the sample.

To address this limitation, single-cell RNA sequencing (scRNA-seq) techniques emerged[14,15]. These methods involve dissociating tissue into individual cells and isolating each cell. Specific barcodes are then added to identify the mRNA sequences of each cell. This approach provides a high-resolution view of gene expression, allowing researchers to study the transcriptomes of individual cells and uncover cellular heterogeneity, identify rare cell populations, and understand cellular development and differentiation pathways. On the other hand, by dissociating the tissue we were losing the spatial information of these cells making it challenging to know which subpopulations of cell types were interacting with each other and how their spatial context influences their function.

In 2016, Spatial Transcriptomics was introduced to address this challenge[16]. This technique combines high-throughput RNA sequencing with spatial information, allowing researchers to map gene expression patterns within the context of the tissue architecture. By preserving the spatial context of the tissue, this method can identify simultaneously the number of transcripts and their spatial locations within the same tissue section. This provides a more comprehensive understanding of cellular interactions and organization. Spatial Transcriptomics has enabled the study of complex tissues such as the brain, tumor microenvironments, and developing embryos, revealing how cells interact within their native environments and contributing to a deeper understanding of tissue biology and pathology[17].

1.2 Evolution of Spatial Transcriptomics platforms

Prior to the development of the current spatial transcriptomics era, researchers used methods like immunohistochemistry and *in situ* hybridization to examine gene expression within tissues. Immunohistochemistry uses antibodies to detect proteins, whereas *in situ* uses labeled RNA or DNA probes to find targeted mRNA sequences within fixed tissues. These techniques were restricted by low multiplexing capabilities, which made it possible to study only a limited small number of genes or proteins at a time, even though they provided useful spatial information[18,19].

The first high-throughput spatial transcriptomics technique was introduced by *Ståhl et al.* [16] in 2016, marking a significant advancement in the field. This method, often referred to as the "spatial transcriptomics" method, used spatially barcoded oligonucleotide probes affixed to glass slides. Tissue sections were placed on these slides, and mRNA released from the tissue was captured by the probes, preserving spatial information. This approach allowed for the simultaneous analysis of thousands of genes across entire tissue sections, representing a major advancement over traditional methods.

The integration of microfluidics and NGS technologies further propelled the field of spatial transcriptomics. Platforms such as Slide-seq[20] and HDST (High Definition Spatial Transcriptomics)[21] emerged, utilizing bead-based capture systems to enhance spatial resolution and throughput. For instance, Slide-seq uses barcoded beads deposited on a slide to achieve near-single-cell resolution, enabling high-resolution mapping of gene expression in complex tissues like the mouse brain.

Recent advancements have focused on combining spatial transcriptomics with single-cell and single-nucleus RNA sequencing. Techniques like MERFISH (Multiplexed Error-Robust Fluorescence In Situ Hybridization)[22], seqFISH (Sequential Fluorescence In Situ Hybridization)[23], Xenium[24] and CosMx[25] have pushed the boundaries of multiplexing, allowing for the spatial profiling of hundreds to thousands of genes at sub-cellular resolution. These methods employ iterative rounds of hybridization and imaging to detect multiple RNA molecules within individual cells, providing an unprecedented level of detail.

1.3 VISIUM

VISIUM[26] from 10xGenomics is the commercial product most demanded in this field that relies on NGS. This platform relies on the use of spatially barcoded mRNA-binding oligonucleotides. Within a VISIUM slide, there are 4 captured areas with a grid of 6.5 mm x 6.5 mm which contains ~ 5000 spots with spatially barcoded mRNA-binding oligonucleotides. The resolution of the spots does not achieve single-cell resolution since the diameter of the spots is 55 µm and the distance between the centers of adjacent spots is 100 µm (**Figure 1**). In fact, the major limitation of this technology is the resolution since we can find on average 1-10 cells within a spot (depending on the tissue type) and there is a large area between spots where the transcriptomic profile of the cells will not be captured.

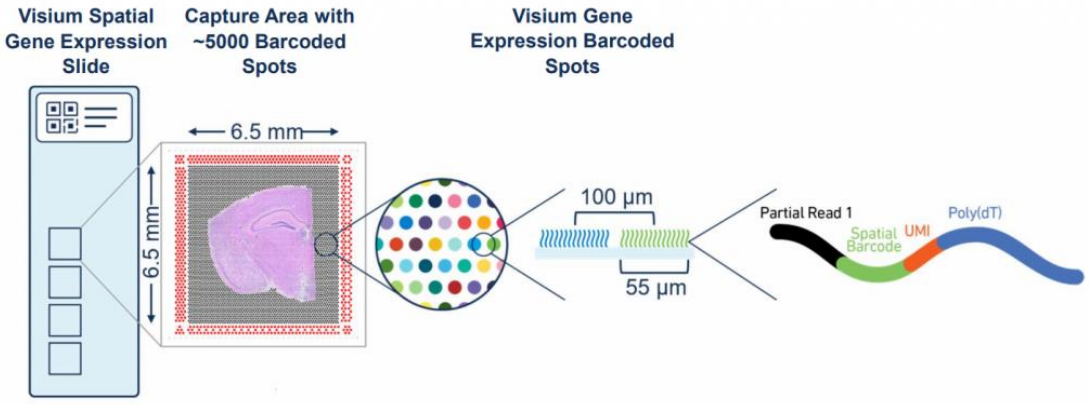

Figure 1 - The Visium Spatial Gene Expression Slide *(https://www.10xgenomics.com/)*

Despite this main drawback, this technology allows the use of two different tissue preservation methods in their protocol: fresh-frozen and formalin-fixed, paraffin-embedded (FFPE). In the fresh-frozen, the whole transcriptome is targeted with no probes, including non-coding genes, since the cDNA is transcribed after the permeabilization of the tissue to the slide. On the other hand, RNA from FFPE samples is less accessible and is fragmented.

Therefore, probes targeting specific genes are needed for a major sensitivity and specificity. This probe set (v1) created by 10x Genomics, targets all protein-coding genes excluding mitochondrial, ribosomal and non-coding genes. For that reason, apart from needing a deparaffinization and rehydration process, there is a probe hybridization and ligation process before permeabilization.

In addition to simultaneous capture of gene expression and the spatial coordinates, there is an imaging process before barcoding which allows to recover tissue morphology to map afterwards with the spatial location of the transcripts. Usually, hematoxylin and eosin (H&E) staining is used because the cell nuclei stains in blue and cytoplasm, extracellular matrix, and other tissue components in pink, recovering the tissue architecture. There is also the option of doing immunofluorescence of a few proteins that can serve to analyze alongside the whole transcriptomic profile.

In the past few years. 10x Genomcis released VISIUM CytAssist to overcome some issues that the previous manual protocol was struggling. For instance, now there is a physical tool that allows the assisted placement of the tissue section on the VISIUM slide when running the protocol but reducing the throughput from four to two samples per slide (with the option of using a large capture area of 11mm x 11mm). Moreover, they have modified the probe set used FFPE samples, now three probes target the same gene instead of one, letting the analysis of samples with more degraded RNA (DV200 > 30% instead of 50%). And the most important change regarding the lateral diffusion of RNA molecules that many users have experienced in the manual VISIUM and now with the CytAssist is solved. Furthermore, this new version of VISIUM allows the simultaneous capture of gene expression and protein expression of (35 proteins) by using primary antibodies specific to the target proteins that are conjugated with oligonucleotides. These oligonucleotide tags include unique sequences that can be detected later during sequencing.

After the sequencing, in order to process the data for creating the count matrices containing the transcriptional profiles and the coordinates, 10x Genomics provides the Space Ranger workflow (**Figure 2**). In brief, extraction of spatial barcodes, unique molecular identifiers (UMIs), and gene sequences from the FASTQ files. Spatial barcodes are mapped to the image fiducial frame specific to the slide. Gene sequences and UMI are mapped to the reference

genome to create the count matrix. VISIUM manual and VISIUM CytAssist follow the same approach.

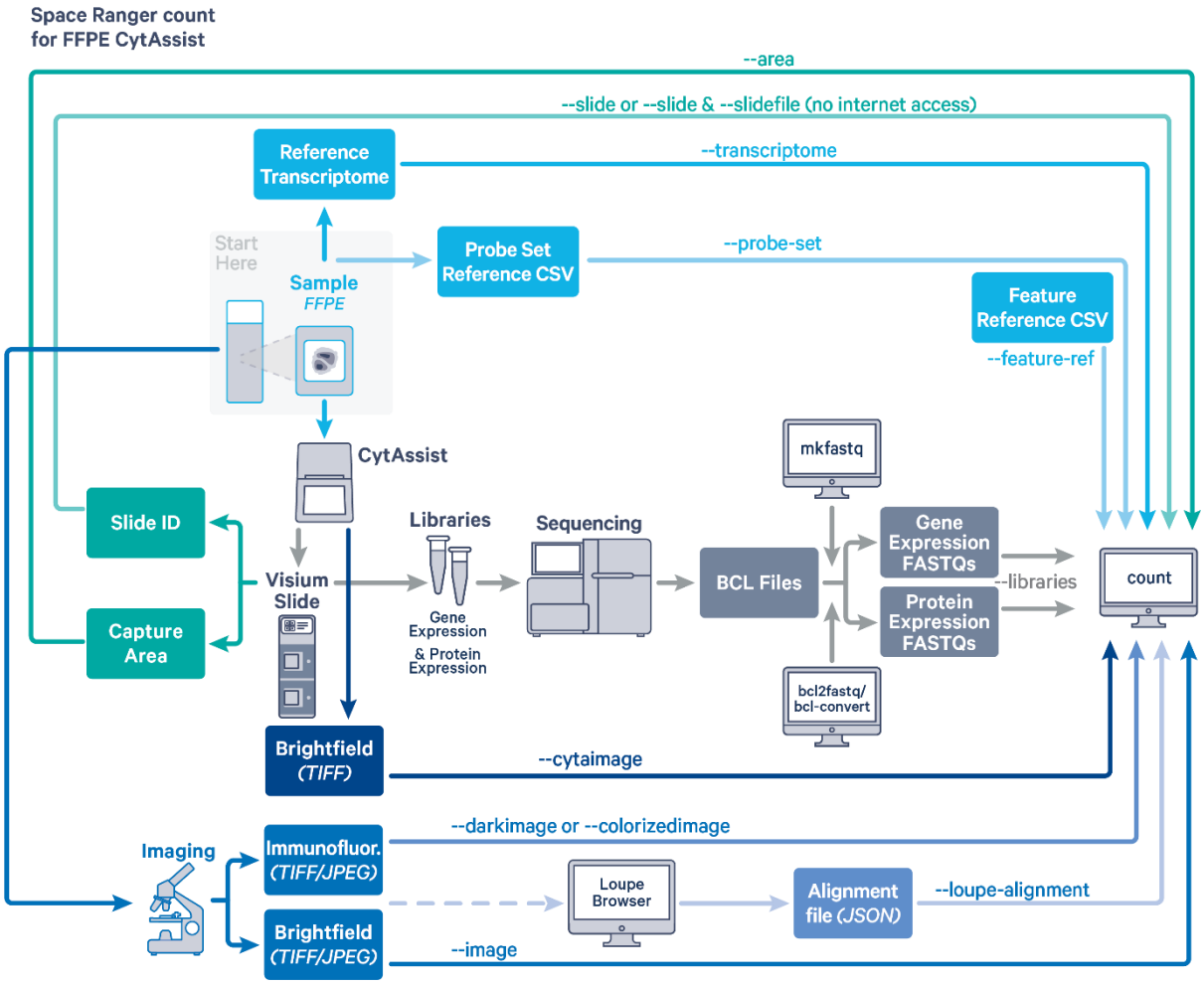

Figure 2 - Space Ranger workflow for CytAssist (Gene and Protein expression)
(https://www.10xgenomics.com/)

1.4 Xenium

Xenium is a cutting-edge spatial genomics platform developed too by 10x Genomics which proposes to achieve high-resolution, multiplexed *in situ* RNA profiling within tissue sections. Xenium combines the latest in microfluidics, advanced imaging, and computational analysis to provide detailed spatial maps of gene expression at the sub-cellular level, within tissue context.

The Xenium workflow (**Figure 3**) involves a highly multiplexed *in situ* hybridization technique in two continuous scan areas of 1.1 cm by 2.4 cm per run with no limit of the number of samples. Specific probes are designed to target a large number of mRNA transcripts,

hybridized directly within the tissue section. These probes contain unique molecular barcodes that allow for the identification and localization of each transcript. Moreover, low-abundance transcripts are detectable thanks to amplification (by rolling circle amplification) after the probe hybridization. Then, the tissue sections undergo advanced microscopy techniques which capture detailed images of the tissue for each fluorescence probe that can be detected and quantified in the space.

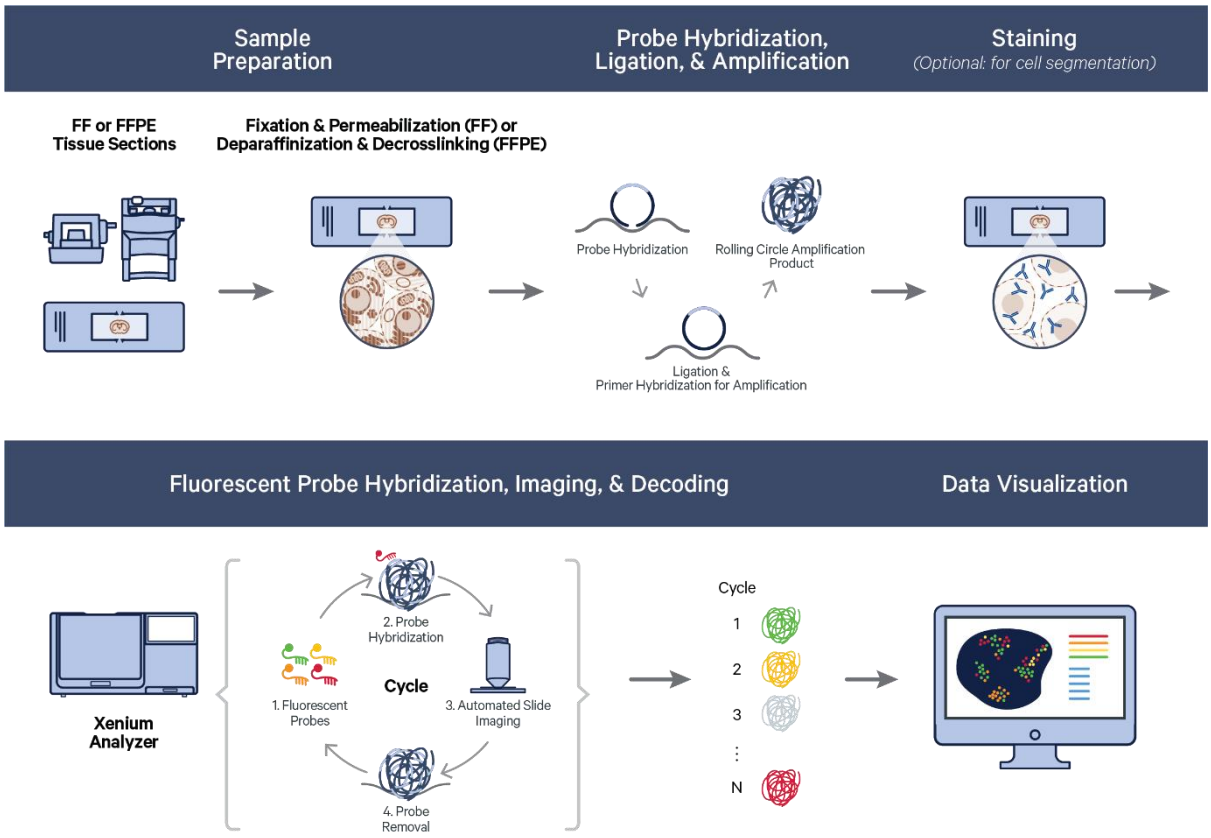

Figure 3 - Xenium workflow *(https://www.10xgenomics.com/)*

The integrated software of the Xenium machine (Xenium Analyzer) uses several algorithms to algin and decode the barcoded signals to map each RNA molecule to its precise location within the tissue. Alongside the RNA expression, there is also a DAPI staining of the tissue to identify the cell nucleus. With the use of nuclear expansion algorithm cells boundaries are segmented making possible the assignment of RNA to specific cells. Moreover, since Xenium protocol does not destroy the tissue, additional H&E imaging from the exact same slice can be performed after.

10x Genomics provides different options for the pre-designed gene panel that will target a few hundred genes. Most of these panels are tissue-specific (lung, breast, brain, liver, colon and skin) and they range from 200 to 300 genes. They also offer multi-tissue (377 genes) or immuno-oncology (380 genes) panels that are widely used by researchers. On top of these panels, there is also the possibility of creating a custom panel at an additional price. At this moment, they support fresh-frozen and FFPE samples for mice and human organisms. Furthermore, these panels provide 20 control probes that ensure the quality of the target probes.

In the Q2 of 2024, 10x Genomics made available a new gene panel that covers 5000 genes instead of a few hundred genes and a multi-modal segmentation kit which improves the cell segmentation.

1.5 CosMx

CosMx from Nanostring is the competitor of Xenium in the *in situ* RNA profiling at the sub-cellular resolution. In terms of concept, it is very close to Xenium workflow with some nuances that can have an impact in the generated data.

The scan area of CosMx (**Figure 4**) is defined by several user-defined fields-of-view (or FOV) that are 0.5mm by 0.5mm with the option of arranging continuously or spreadly over the tissue. Regarding the chemistry, the main difference is the amplification of transcripts. In Xenium, the strategy is rolling circle amplification while in CosMx we have a branched probe hybridization approach. Furthermore, one of the most important aspects of CosMx is its cell segmentation strategy. They use cell membrane and morphology protein markers (PanCK, CD3) alongside DAPI to segment the cell boundaries through machine-learning approaches. The gene spatial map and the cell segmentation are done automatically within the machine (CosMx SMI).

There are fewer gene panels that CosMx offered but with a higher plexity, with the most commonly used of 1000 genes (in humans and mice). On top of this, they can provide the characterization of 100 proteins alongside gene expression profiles.

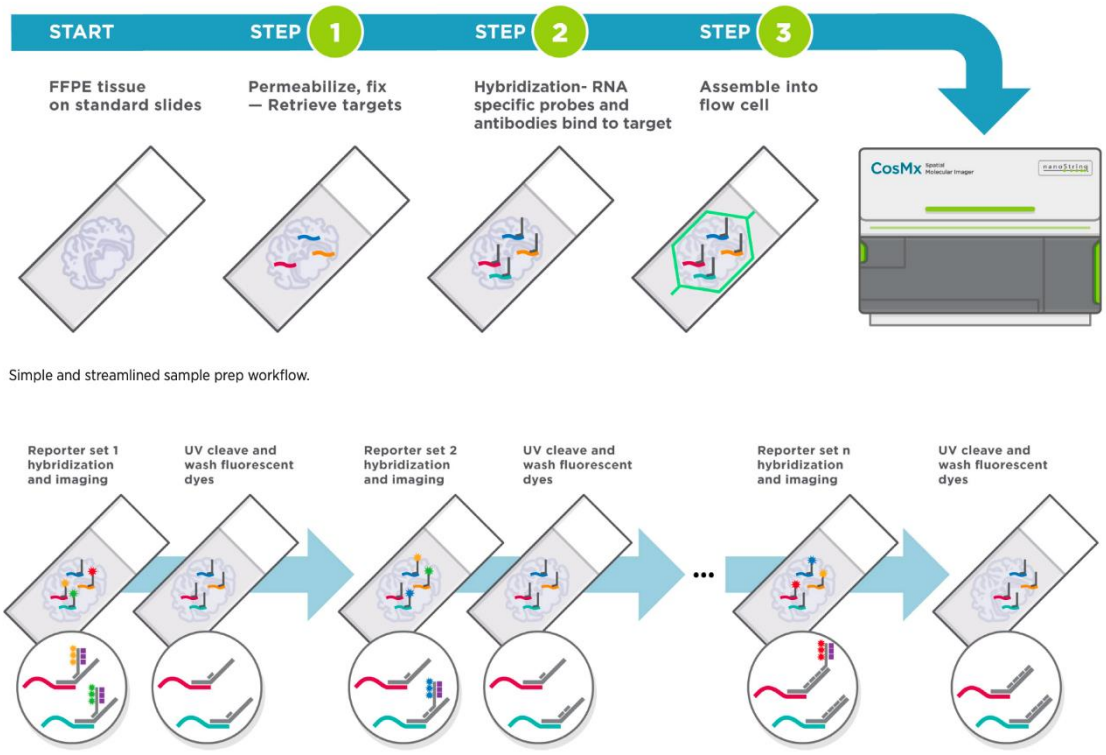

Figure 4 – CosMx workflow *(https://nanostring.com/)*

2. Objectives

To compare the data generated using four different spatial transcriptomics platforms (VISIUM manual, VISIUM CytAssist, Xenium and CosMx) and one spatial proteomics platform (VISIUM CytAssist) across serial sections of six FFPE samples from primary human tumors.

In this comparison, we want to assess the data quality and their impact on the biological interpretation of the samples. Furthermore, we will compare different multi-omics data and quantify how differ from each other.

3. State-of-the-art

As mentioned in the introduction, the spatial field is evolving faster than ever with significant new cutting-edge technologies and improvements in existing protocols. This fact raises the necessity of benchmarking and validating to what extent these results are reliable and useful for research. The first comparisons between new technologies always arise when comparing their product against the competitors. This fact has been already experienced in NanoString and 10x Genomics with their new *in situ* products (CosMx and Xenium, respectively). In the case of CosMx was highlighting its strength in the cell segmentation, therefore a correct

transcript assignment to a cell[27]. While Xenium was emphasizing their reliability of transcript detection. However, this comparison could not be totally fair since there is a conflict of interests and companies will only show their strong points, making clear the need for an unbiased comparison of these technologies.

At the time of designing the experiment and generating the *in situ* data (late 2023), there were no studies from research groups without interest involved when comparing these two platforms. Nevertheless, three new research appeared in December 2023 and January 2024 to fill the missing gap that exists in the field.

In Wang *et al.*[28]**,** they performed a benchmarking of three commercially *in situ* platforms (Xenium, CosMx and MERFISH) across 23 tissue microarrays (TMAs) from FFPE blocks covering seven human tumor types and normal tissues, apart from testing different gene panels. In this study the authors highlight the overall performance of transcript detection, considering the core-level analysis. Furthermore, they show the problem in CosMx samples where lowly expressed genes are not reliable because of the high discovery rate (FDR). In the case of cell segmentation, Xenium showed the poorest results among technologies due to its inherent approach. Finally, in terms of cell type identification, all platforms recovered general cell types but the classification of sub types CosMx was not showing good results.

A week later, Cook *et al.*[29] shows their results where they compared consecutive sections of a prostate adenocarcinoma sample (FFPE) with biological replicates for Xenium (377 genes panel) and CosMx (960 genes panel). In addition, they also generated single-cell data that will be used for validation. Here, the authors reported the high reproducibility between biological replicates in both platforms. In the case of transcript detection, Xenium showed a higher sensitivity and dynamic range compared to CosMx, which also aligned with the results obtained from single-cell data. CosMx had superior cell segmentation to Xenium's with some areas with minimal impact in the cellular transcriptomic profile regarding transcript misassignment. Again, both platforms effectively annotate cell types despite the nosier expression of some markers in CosMx.

The last of them was released in January 2024 by Hartman and Satija[30]. In this study, they provide a complementary point of view to the other two studies since they used data from six different *in situ* platforms (Xenium, MERSCOPE, Molecular Cartography, MERFISH,

STARmap PLUS and EEL FISH) from mouse brain (no matching samples). Their results suggest that MERSCOPE from Vizgen is the best technology in terms of transcriptome coverage and an optimal trade-off between sensitivity and specificity. This was followed by Xenium whose main drawback was the cell segmentation aspect. In addition, they explore in more detail the effects of cell segmentation and the future direction of developing new cell segmentation tools that will overcome transcript misassignment from neighboring cells.

3. Experimental Design

To fairly compare the performance of the distinct spatial platforms, we generated data from consecutive sections from formalin-fixed, paraffin-embedded (FFPE) human blocks covering six of the most common solid tumors: colorectal (adenocarcinoma), breast (infiltrating carcinoma of non-special type), lung (acinar invasive adenocarcinoma), lymphoma (diffuse large B-cell lymphoma), ovarian (high-grade serous carcinoma), and bladder (muscle-invasive bladder cancer).

For only colorectal, breast, lung and lymphoma samples, the first serial sections were used to generate manual VISIUM data. This data was already generated and analyzed in a previous integrative spatial transcriptomics study[31]. Then, there were 5 to 10 (25 to 50µm of depth) discarded sections that are removed since there exists some degradation when preserving the blocks. After this tissue removal, three serial sections were obtained from the six samples and they were used to generate Xenium (Human Multi-Tissue and Cancer panel), CosMx (Universal Cell Characterization RNA Panel) and VISIUM CytAssist (+Proteins). However, the breast sample during the 95ºC decrosslinking step of the CytAssist protocol was partially detached leading to tissue fold. Due to this problem, we decided to discard this sample and replace it with already generated data from the same sample using VISIUM CytAssist with the large capturing area (11.5mm) without protein capture. The section for this data was a consecutive section from the manual VISIUM therefore it is close in space and time compared to the other samples. In **Figure 5** we can observe the schema of the experimental design considering the sections, timepoints and data generated in each modality.

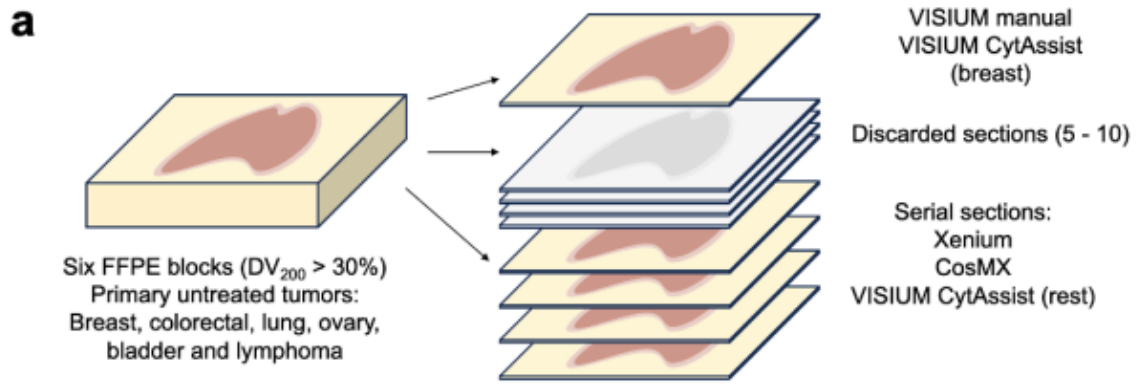

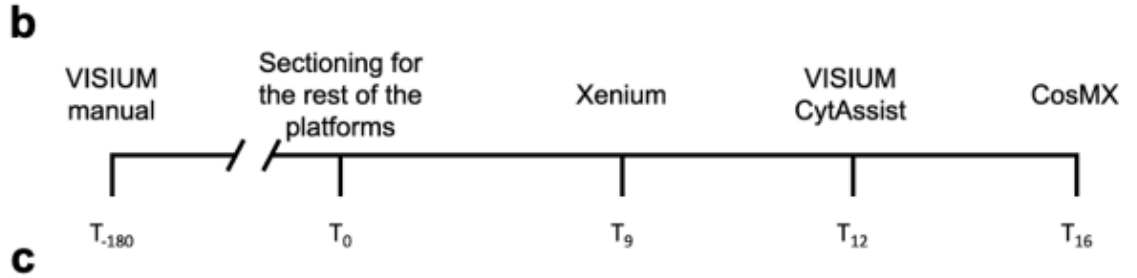

c

Sample	Sequencing-based			Imaging-based	
	VISIUM manual	VISIUM CytAssist		CosMx	Xenium
		GEX (11.5mm)	GEX+PEX (6.5mm)		
Bladder			x	x	x
Breast	x	x		x	x
Colorectal	x		x	x	x
Lung	x		x	x	x
Lymphoma	x		x	x	x
Ovarian			x	x	x

***Figure 5 – Experimental design*. a)** Schematic representation of the tissue section collected in a FFPE block for each of the six tumor types. **b)** Timeline showing the generation of the different datasets. **c)** Table of the samples generated for each technology used in the benchmarking.

4. Methods

Sample acquisition

All experimental procedures and bioinformatic analyses in this work comply with ethical regulations and good scientific practices.

Tissue preparation and sequential sectioning

For our benchmarking purpose, we selected six untreated primary tumor samples, covering the most common cancer types: colorectal, breast, lung, lymphoma, ovarian, and bladder. The H&E staining from each formalin-fixed paraffin-embedded (FFPE) blocks, helped us to

characterize the tissues and confirmed that each sample had an adequate and good quality representation, not only of tumor tissue but also of the surrounding healthy tissue, to warrant the experiments.

First, the quality of preserved RNA in the FFPE blocks was evaluated based on the percentage of RNA fragments above 200 base pairs (DV200). For each block, we sectioned and collected three consecutive 8 µm sections for RNA purification using the RNeasy FFPE kit for RNA Purification (Qiagen Cat No: 73504). We analyzed the purified RNA with Agilent tapestation, and chose the samples with values above 34% of DV200. The dimensions of the tissue in the selected blocks were approximately 7 mm by 7 mm, except in the bladder sample that the block was formed by small pieces of tissue from the same patient.

To facilitate a comprehensive comparison of data from VISIUM manual, Xenium, CosMx, and VISIUM CytAssist platforms, we sectioned the chosen samples as illustrated in Figure X.

More in detail, from each of these samples we had collected and processed one 7um section for VISIUM manual analysis 6 months ago, and we had stored the blocks at 4 degrees. For the benchmarking study we retrieved the blocks, discarded between 5 to 10 - 5um sections and collected three 7 µm serial sections for Xenium, CosMx, VISIUM CytAssist analysis and one extra for H&E staining.

The sectioning was conducted using a semi-automated microtome (ThermoScientific HM340E), utilizing a fresh blade and ensuring thorough decontamination with RNAse AWAY (ThermoFisher Scientific). We detail the sectioning and subsequent slide preparation methods for Xenium, CosMx and VISIUM CytAssist platforms in each chapter.

Xenium sample preparation

The Xenium workflow began by sectioning 7µm FFPE tissue sections onto a Xenium slide, according to the "Xenium In Situ for FFPE- Tissue Preparation Guide" (CG000578 Rev C, 10X Genomics). Briefly, the sections were cut, floated in an RNAse-free water bath at 42 degrees, and carefully placed onto the capture area of a Xenium slide (PN- 1000465). We strategically placed three 7x 7mm sections in each slide. After sectioning, the slides were incubated at 42 degrees per 3 hours, and kept in a sealed bag with desiccators at 4 degrees overnight. The

next day, the slides were shipped to the Dresden Genome Center Facility, where the experiments were conducted.

At the Dresden Genome Center Facility, the Xenium slides were processed following the "Xenium In Situ for FFPE- Deparaffinization and Decrosslinking" protocol (CG000580 Rev C, 10X Genomics). The slides were equilibrated to room temperature and the protocol of deparaffinization was performed.

Subsequently, the Xenium slides were assembled into Xenium cassettes (PN-1000566, 10X Genomics), which allow for the incubation of slides on the Xenium Thermocycler Adapter inside a Thermocycler machine with a closed lid for optimal temperature control. The slides were processed using the "Xenium Slides and Sample Prep Reagents" kit (PN-1000460, 10X Genomics), starting with incubation in a decrosslinking and permeabilization solution at 80°C for 30 minutes, followed by a wash with PBS-T.

The Xenium slides were then processed according to the "Xenium In Situ Gene Expression" user guide (CG000582 Rev D, 10X Genomics). The slides were incubated at 50°C overnight for aproximately 19 hours with the gene expression panel ("Xenium Human Multi-Tissue and Cancer Panel", PN-1000626, 10X Genomics, which targets 377 human genes). This was followed by a series of washes and steps, including a post-hybridization wash at 37°C for 30 minutes, a ligation at 37°C for 2 hours, and an amplification step at 30°C for 2 hours. After additional washing steps, the slides were treated with an autofluorescence quencher and a nuclei staining step.

Finally, at the end of the second day of the protocol, the two slides in the cassettes were loaded into the Xenium Analyzer. The first step in the instrument consists in a sample scan, were images of the fluorescent nuclei in each section are given, and these images allow the user to select and determine the regions to be included in the analysis. For the 6 samples, we selected all the tissue to be analyzed.

The run in the Xenium Analyzer lasted around 50 hours. After that, the instrument was emptied of consumables and the Xenium slides carefully removed. PBS-T was added to the slides and a post-run H&E staining was performed.

Visium CytAssist whole transcriptome and protein panel

Visium CytAssist with the protein panel provides whole transcriptome, spatially-barcoded sequence data. The histology workflow was performed using the Visium CytAssist Spatial Gene Expression for FFPE (Demonstrated Protocol CG000520). The tissue was sectioned as described in Visium CytAssist Spatial Gene Expression for FFPE – Tissue Preparation Guide (Demonstrated Protocol CG000518). 7 µm sections were placed on a Microscope Slide, stained for H&E and deparaffinize. Samples were imaged using a Nikon microscope, the coverslip was removed, followed by hematoxylin destaining and decrosslinking (Demonstrated Protocol CG000520). The glass slide with tissue section was processed with a Visium CytAssist instrument to transfer analytes to a Visium CytAssist Spatial Gene Expression slide with 6x6mm capture areas.

The library construction for gene and protein expression was done following 10x genomics User Guide CG000494. briefly after probe ligation, samples were incubated with the protein panel, and two libraries were generated per sample.

GEX and PEX Libraries were sequenced with paired-end dual-indexing (28 cycles Read 1, 10 cycles i7, 10 cycles i5, 50 cycles Read 2). Sequencing libraries were demultiplexed with bcl2fastq (Illumina). The Space Ranger pipeline v2022.0705.1 (10x Genomics) and the GRCh38-2020-A reference were used to process FASTQ files.

CosMx data generation

The FFPE blocks from each sample were sectioned as described in CosMx Tissue Preparation Guide (MAN-10184-02, Nanostring). Briefly, 7 µm sections were cut, floated in an RNAse-free water bath at 42 degrees, and carefully placed onto the center of a Microscope Slide (Superfrost Plus, Epredia J1800AMNZ), considering the specific area the CosMx instrument can analyze. After sectioning, the slides were incubated at 42 degrees per 3 hours, and kept in a sealed bag with desiccators overnight. The slides were shipped to NanoString Seattle for profiling as part of their early technology access program (TAP).

Once in Seattle, the slides were processed following Nanostring MAN-10184-02. Briefly, the samples were baked overnight at 60 °C, followed by preparation for in-situ hybridization (ISH)

on the Leica Bond RXm system by deparaffinization and heat-induced epitope retrieval (HIER) at 100 °C for 15 min using ER2 epitope retrieval buffer (Leica Biosystems product, Tris/EDTA-based, pH 9.0). After HIER, tissue sections were digested with 3 µg/ml Proteinase K diluted in ACD Protease Plus at 40 °C for 30 min.

Tissue sections were then washed twice with diethyl pyrocarbonate (DEPC)-treated water (DEPC H2O) and incubated in 0.00075% fiducials (Bangs Laboratory) in 2X saline sodium citrate, 0.001% Tween-20 (SSCT solution) for 5 min at room temperature in the dark. Tissue sections were fixed with 10% neutral buffered formalin (NBF) for 5 min at room temperature. Fixed samples were rinsed twice with Tris-glycine buffer (0.1 M glycine, 0.1 M Tris-base in DEPC H2O) and once with 1X PBS for 5 min each before blocking with 100 mM N-succinimidyl (acetylthio) acetate (NHS-acetate, Thermo Fisher Scientific) in NHS-acetate buffer (0.1 M NaP, 0.1% Tween pH 8 in DEPC H2O) for 15 min at room temperature. The sections were then rinsed with 2X saline sodium citrate (SSC) for 5 min and an Adhesive SecureSeal Hybridization Chamber (Grace Bio-Labs) was placed over the tissue.

NanoString ISH probes were prepared by incubation at 95 °C for 2 min and placed on ice, and the ISH probe mix (1 nM 980 plex ISH probe, 10 nM Attenuation probes, 1 nM SMI-0006 custom, 1X Buffer R, 0.1 U/µL SUPERase•In™ [Thermo Fisher Scientific] in DEPC H2O) was pipetted into the hybridization chamber and hybridization was performed at 37 °C overnight. Tissue sections were washed twice in 50% formamide (VWR) in 2X SSC at 37 °C for 25 min, washed twice with 2X SSC for 2 min at room temperature, and blocked with 100 mM NHS-acetate in the dark for 15 min. In preparation for loading onto the CosMx SMI instrument, a custom-made flow cell was affixed to the slide.

RNA target readout on the CosMx SMI instrument was performed. Briefly, the assembled flow cell was loaded onto the instrument and Reporter Wash Buffer was flowed to remove air bubbles. A preview scan of the entire flow cell was taken, and 40-58 fields of view (FOVs) were placed on the tissue to match regions of interest. RNA readout began by flowing 100 µl of Reporter Pool 1 into the flow cell and incubation for 15 min. Reporter Wash Buffer (1 mL) was flowed to wash unbound reporter probes, and Imaging Buffer was added to the flow cell for imaging. Nine Z-stack images (0.8 µm step size) for each FOV were acquired, and photocleavable linkers on the fluorophores of the reporter probes were released by UV

illumination and washed with Strip Wash buffer. The fluidic and imaging procedure was repeated for the 16 reporter pools, and the 16 rounds of reporter hybridization-imaging were repeated multiple times to increase RNA detection sensitivity.

Data preprocessing of sequencing-based technologies

Transcript count matrices from SpaceRanger were imported with Seurat[32] (v5). Spots were filtered based on their location since there were spots detected out of the tissue or in folded areas with misleading gene expression. Furthermore, genes with less than five transcripts in the whole tissue were discarded. Given that for the Breast sample we used the 11.5 mm capture area, we subset the tissue for a fairer comparison with the manual VISIUM. Then, the gene expression was normalized using the SCTransform function from Seurat.

For CytAssist samples with a protein panel, the protein expression was imported into a new assay independently of the gene expression. No additional spots or proteins were filtered out. Finally, the protein expression was normalized using the centered log ratio (CLR) method implemented in Seurat.

Data preprocessing of image-based technologies

Gene expression profiles matrices from Xenium Analyzer (v1.5.0.3) of each sample were imported using Seurat (v5). Since the CosMx run aggregated all samples within a single TileDB object, we proceeded to segregate and import each individual sample into a Seurat object based on their respective slide coordinates. During the preprocessing, only cells with no transcripts were filtered. In addition, cells of CosMx that were found in the “Barrel effect” area (see Barrel effect section) were excluded for all comparative experiments. Finally, gene expression was normalized using the SCTransform function from Seurat.

Image registration across platforms

Because we did not have a whole tissue image for CosMx, we could not apply Image Registration techniques to transfer the coordinates of Xenium to the CosMx. Therefore, we aligned the images by first applying a rotation angle to the Xenium coordinates that was defined by overlaying the distribution of centroids in the space in an image editor software. In the case of the Bladder sample, we had to separate the tissue regions as they could differ

in orientation and distance. Then we shifted the x and y coordinates of CosMx (since they covered less tissue area) based on common landmarks defined by tissue morphology. Angles and shifting specific for each sample can be found in the code. After that, from the Xenium samples were subset by the limits of each FOV in the CosMx as well we discarded CosMx cells that were not found in the Xenium samples.

In the case of the alignment between CytAssist and Xenium/CosMx, we applied Image Registration using the software Voltron[33] by defining landmarks between Xenium (DAPI) and CytAssist (H&E) images. Then the transformation was applied in the CytAssist spot coordinates to use them in the Xenium space, so we could transfer the FOV limits and subset.

Barrel effect

Cells that suffered from the "Barrel effect" in CosMx are found in 36px (4.33 um) from the edge of the FOV. To compare the gene expression in these cells with the rest of the FOV, we subsetted those cells whose centroid coordinates (x or y) concerning the FOV is smaller than 36 or bigger than 4220. Furthermore, to ensure that the differences that we found could be related to the subsetting, we selected an area similar to the barrel effect in the middle of the FOV (between 2000 and 2100 px).

False Discovery Rate

False Discovery Rate (FDR) in each platform and sample was computed using the following formula:

$$\frac{\sum_c Control_c}{\sum_c Control_c + \sum_g Gene_g} \; x \; \frac{G}{C} \; x \; 100$$

where C is the total number of negative controls (10 in CosMx vs 20 in Xenium), G is the number of genes in the panel (1000 vs 377, respectively), Control is the sum of the negative control c and Gene is the gene expression of gene g.

Spatial Autocorrelation

To quantify the spatial variation of the normalized transcripts we use global Moran's I metric. In sequencing-based methods, we used the function CorSpatialFeature from semla package[34]

considering the six closest spots as neighbors (default). For image-based technologies, the function RunMoransI from the package Voyager[36]. In this case the spatial network was built using the five closest neighbors considering centroid distances

FindSpatialNeighbors(method="knearneigh", dist_type="idw", k=5, style="W").

For estimating the spatial clustering of cell identities, the same approach was applied by transforming the categorical data into one hot encoding.

Cell annotation

To annotate image-based sequencing data without reference data, we use SingleR package[35] to map the annotations of the following cell types: Epithelial, Endothelial, Fibroblast, Smooth muscle, Macrophage, Monocyte, DC, Neutrophil, NK cell, B cell, immature B cell, memory B cell, naive B cell, plasma B cell, CD4+ T cell, CD8+ T cell, effector T cell and Treg. The "HumanPrimaryCellAtlasData" was used as reference and the normalized data with SCT was used as input. Cells with labels NA after the pruning were discarded in the comparison of the technologies.

FOV sampling experiment

To evaluate the influence of cell type composition within a selected portion of the tissue, we conducted a sampling experiment. Initially, we treated the CosMx FOV size (0.5 mm x 0.5 mm) in the Xenium (shared area) sample as a single unit to facilitate stochastic sampling while adhering spatial constraints. Additionally, we sampled the same number of cells that appear on average in a FOV simulating a single-cell experiment without spatial constraints. Subsequently, we performed 100 iterations of sampling across various quantities of FOVs, including 1, 5, 10, 20, 40, and the maximum number of FOVs possible within the given sample. For each sampling iteration, we calculated the relative abundance of three grouped cell types: Cancer (epithelial), Stroma cells (Fibroblasts, Smooth Muscle and Endothelial cells), and Immune cells (the remaining cell types).

Transferring Xenium information to CytAssist spot resolution

After the image registration between Xenium and CytAssist samples, we transfer the coordinates of CytAssist spots to the Xenium space. Then, for each spot, we assigned the cells within a radius of 27.5 µm to the spot center. Finally, for the deconvolution we computed the relative abundance of each cell type from the assigned cells. For the gene expression, we aggregated the sum of gene transcripts found within each spot and we normalized using SCTransform.

CPTAC protein and RNA analyses

We downloaded the CPTAC protein and RNA expression matrixes from Liang *et al.*[36]. Then, for each gene included in the 10x Genomics CytAssist protein panel, we calculated the correlation coefficient between the bulk RNA counts and the mass-spectrometry protein expression data across all 10 cancer types included in the CPTAC study using a linear model.

5. Results

5.1 Comparison of sequencing-based platforms

The generation of data from manual VISIUM and CytAssist protocols show, overall, the vast majority of genes (~15.000) are consistently detected using both chemistries (**Figure 6a**), however, CytAssist tends to have more uniquely detected genes (around 2.000) than VISIUM manual (around 200), consistent with the fact that VISIUM CytAssist has three probes per gene instead of only one. Similarly, the number of detected genes (**Figure 6b**) and UMI per spot, considering that a spot can contain 1-10 cells depending on the tissue type, also tends to be higher in CytAssist than in the VISIUM manual. Also, it is important to note that in the new version of probes used in CytAssist there are almost 600 genes different from the previous version due to lack of specificity in the previous version. Interestingly, in the CytAssist there are specific probes that target mitochondrial genes whereas in VISIUM manual we cannot quantify it for FFPE samples.

Apart from the total number of detected genes in each sample and platform, we checked if the same number of UMIs per gene was similar by computing the median UMIs per gene in all spots. For instance, in the lung tumor sample (**Figure 6c**) we find a very high correlation

between manual and CytAssist, showing a strong similarity UMI per gene detection and no gene with a strong bias. However, in the range of lower median gene expression (<0.1) we find a significant fraction of genes with higher UMI counts detection in CytAssist. When exploring this across all samples, between 25% and 30% of genes had at least twice as many median UMIs in CytAssist than in manual VISIUM (**Figure 6d**), whereas only between 2% and 6% had the opposite pattern, being the lymphoma sample the tumor with higher fraction for manual VISIUM.

Finally, we quantified how the gene expression was detected across the space by computing the randomness of the spatial distribution through the global Moran's I metric. This is important since tissues are spatially structured, and many genes follow a spatial pattern that tends to be cell-type specific. Thus, by exploring the spatial clustering of gene expression, again, in the lung tumor sample (**Figure 6e**), there exists a correlation between both protocols, but we find some genes that exhibit a spatial pattern (higher Moran's I) in one platform but not in the other. Putting the threshold at a Moran's I 0.1 value higher in one of the two platforms, only between 0.5% to 7% of genes have a higher value in VISIUM manual, whereas between 19% to 27% do for the CytAssist (**Figure 6f**).

This higher clustering with the CytAssist version of VISIUM can be seen in the expression pattern of *ACTA2* in the colorectal cancer sample (**Figure 6g**). This gene, which is associated mainly with the presence of fibroblasts and smooth muscle cells[37], overlaps the fibrotic area of the sample in both platforms, but the non-fibrotic area in the case of manual VISIUM also shows some degree of expression, suggesting a noisier pattern with potential false positives due to lateral diffusion of RNA. Overall, our results show that the use of CytAssist, along with variety of platforms available, the changes in the chemistry of the reagents, have led to a significant improvement in the data generated by VISIUM.

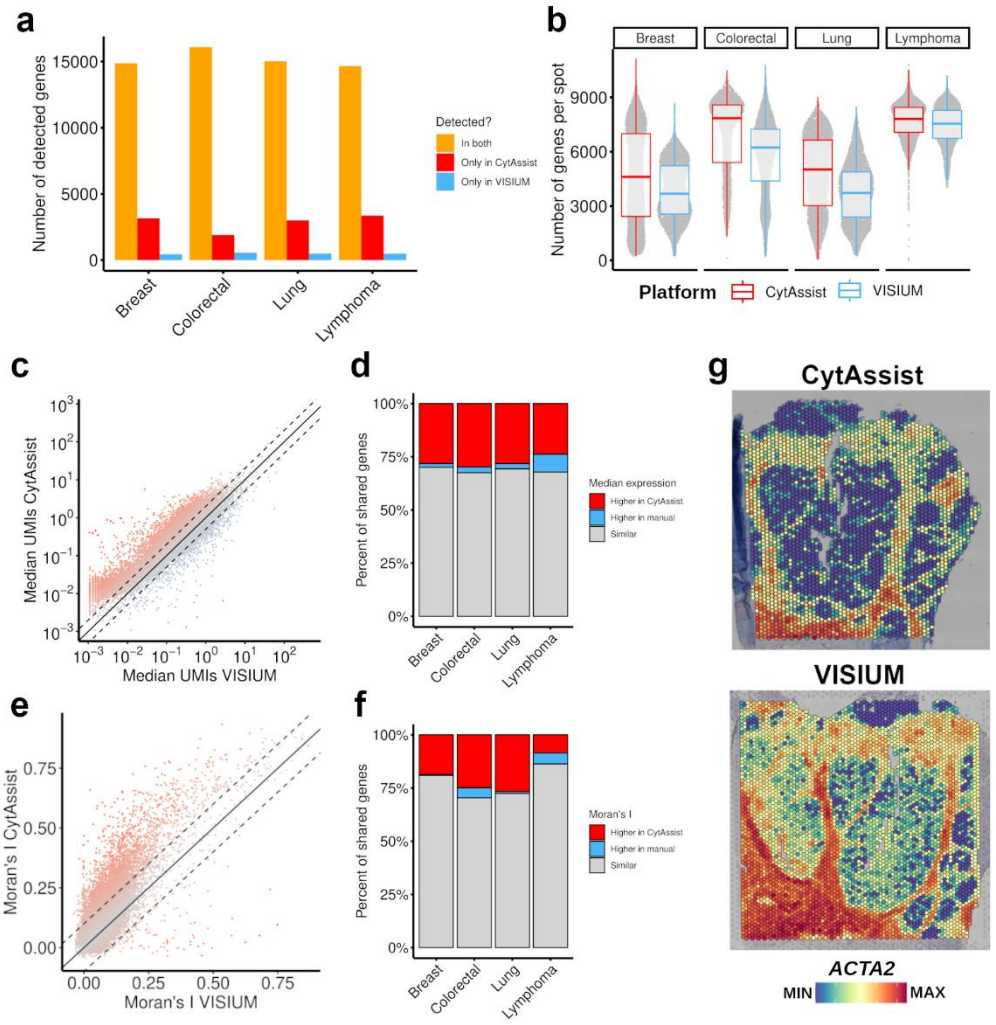

Figure 6 – Comparison of VISIUM manual and CytAssist. **a)** Barplot of the number of detected genes in each sequenced-based platform colored by shared and unique genes. **b)** Distribution of the number of unique genes detected in each spot across samples and platforms. **c)** Scatter plot of median UMI per genes in VISIUM and CytAssist in the Lung sample. Color intensity of dots represents the distance from the diagonal (equal UMI detection across platforms). **d)** Barplot showing the relative number of genes that have similar numbers of transcripts or are higher in one platform for each sample. **e)** Scatter plot of global Moran's I for each gene in VISIUM and CytAssist in the lung sample. Color intensity of dots represents the distance from the diagonal (equal UMI detection across platforms). **f)** Barplot showing the relative number of genes that have similar spatial distribution or are higher in one platform for each sample. **g)** Gene expression of ACTA2 of the colorectal sample using CytAssist (top) and VISIUM (bottom).

5.2 Technical differences of *in situ* platforms

An emerging alternative to sequencing-based spatial transcriptomics are platforms based on *in situ* transcript quantification. These rely on fluorescent probes and high-resolution imaging to capture the precise location of individual mRNA molecules at subcellular resolution, which are then assigned to individual cells using cell segmentation approaches. There is currently a

variety of platforms available, but here we focused on two of the more widely-used: CosMx (from Nanostring) and Xenium (from 10x Genomics).

While the general concept of both platforms is similar, there are important differences that need to be considered before any comparison can be made. For example, neither platform generates (yet) whole transcriptome data but, instead, they focus on gene panels. In the case of Xenium, we used the human multi-tissue panel which includes 377 genes, whereas for CosMx we used the 1000 genes panel. Both platforms also differ in the details of how they acquire the data. While Xenium can scan a continuous area of 1.1 cm by 2.4 cm, CosMx scans several user-defined fields-of-view (or FOV) that are 0.5mm by 0.5mm. In our case, we scanned an average of 58 FOVs per sample with CosMx (totaling 87.5 mm^2 for all samples), whereas we scanned 394.7 mm^2 with the Xenium. In our samples, we captured significantly more cells in Xenium for each sample than with the CosMx (**Figure 7a**), considering that the running time for each platform was three days and two weeks, respectively.

On the same line, CosMx instrument has an important artifact on its FOVs, where cells that are at 4.33um (or 36px) from the border have an order of magnitude less UMIs counts than cells in the inner area of the FOV in all samples (**Figure 7b**). This phenomenon is known as the "barrel effect" and is due to optical distortion making a decrease of the magnification towards the edges of the image[38]. Then, when the different z-stack layers must be aligned there is a full reconstruction of the gene expression as we would expect. Furthermore, we also have to consider that there is no stitch between adjacent FOV, thus it is more likely to find partial cells found in the edge area with lower gene expression than fully captured cells.

To limit the impact of tissue selection bias that exists between the platforms, we only considered the shared areas after image registration to have more fair comparison (**Figure 7c**), since different cell compositions could bias the interpretation of the differences to compare between them. The number of cells in the shared areas of each sample converged toward similar values, even if Xenium still has an average of 5% to 30% more cells (**Figure 8a**). The only extreme case was the lymphoma sample, where we found more than 20000 cells of difference triggering if this difference was due to the technical differences between cell segmentation. In the case of Xenium, it uses DAPI to identify the nucleus and then expands

the perimeter to identify the solution that best limits the space occupied by each cell. On the other hand, CosMx relies on both, DAPI staining for the nucleus, as well as membrane staining,

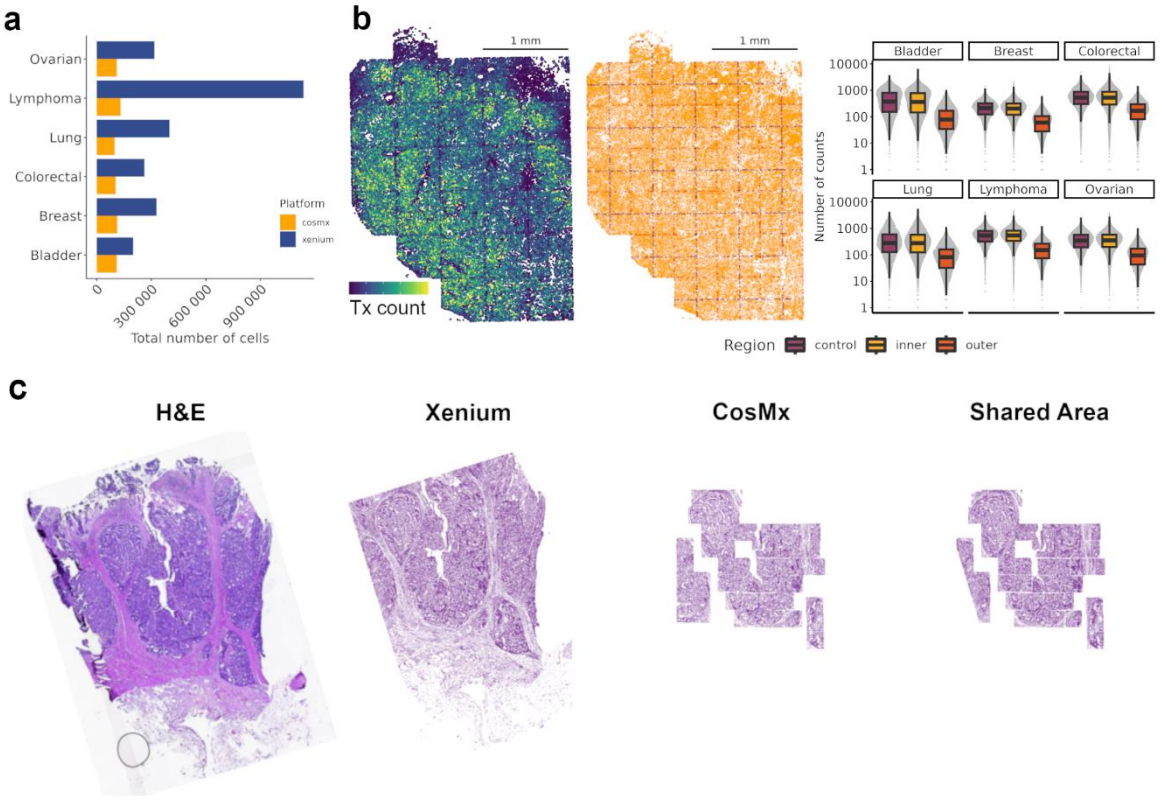

***Figure 7* – Main differences between in situ platforms. a)** Barplot of the number of detected cells in each image-based platform (whole scanned area). **b)** The left plot shows the number of transcripts detected per cell in a small area of the Bladder sample in CosMx. The middle plot shows the cells in the Bladder sample (CosMx) colored according to their distance to the FOV edge: in red the control (between 2000 and 2100 px), in orange the outer area (36px from the edge), and the remaining cells in yellow. The right boxplot shows the number transcripts detected in each cell and in each CosMx sample. **c)** Representation of the colorectal tissue analyzed and compared: hematoxylin and eosin from a section of the FFPE block (first), cells captured using Xenium (second), cells captured using CosMx (third) and cells that are in the shared regions between Xenium and CosMx (fourth).

identifying both cell compartments. This created a less robust cell morphology in Xenium with these inflated or round shapes in low cell density areas (**Figure 8b**). We observed that cells analyzed with Xenium are, on average, bigger than in CosMx in all samples but lymphoma where we had much more cells detected in Xenium (**Figure 8c**). Moreover, extreme outliers with a larger area of 1000 µm² were also found in Xenium, suggesting areas of lower density of cells a freedom to expand the segmentation. Finally, we did not explore more in detail the segmentation differences across platforms because we did not have a ground truth to validate the correctness of transcripts assignment and due to differences of confidence in transcript

detection across platforms (that we will explore later), we could not quantify the co-expression of mutually exclusive genes.

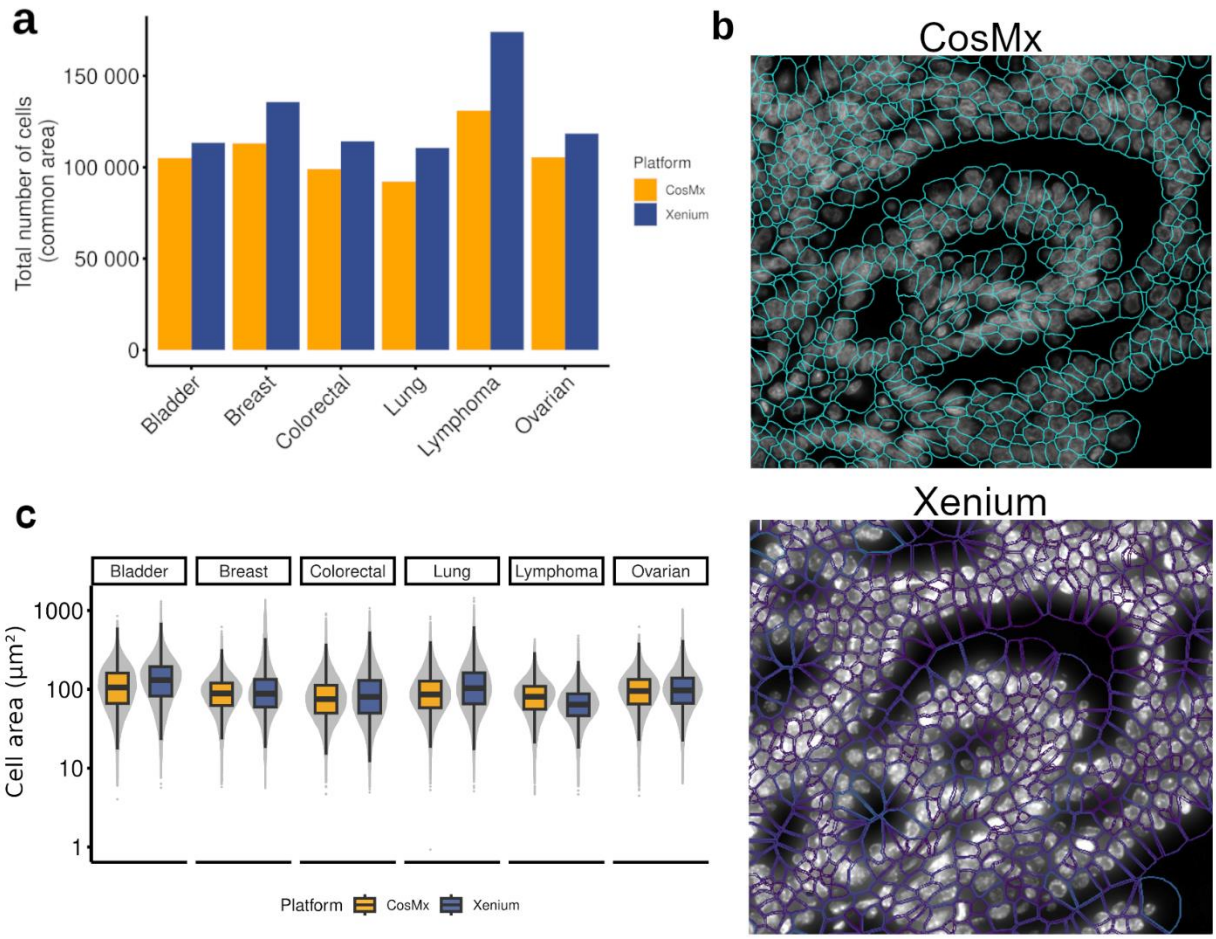

Figure 8 **– Cell segmentation differences between in situ platforms. a)** Barplot of the number of cells within the shared regions between CosMx and Xenium in the different tumor types. **b)** Cell segmentation boundaries of a zoomed area of the breast tumor sample in CosMx (top) and Xenium (bottom) **c)** Boxplot comparing the distribution of the cell area (µm²) in CosMx and Xenium.

In the case of transcript detection, we explored the differences considering the whole gene panel (377 in Xenium and 1000 in CosMx) and then the differences considering only the overlapping genes (n=125). In terms of the whole panel, we found that the percentage of unique genes found in a cell in each panel was on average in CosMx ~20% and Xenium ~10%, however, we found less variability in Xenium across cells compared to CosMx (**Figure 9a**). Similarly, we can see this tendency in the total number of transcripts normalized by the gene panel size where some samples exhibit larger differences across technologies (**Figure 9b**)**.** Despite the higher number of captured transcripts in CosMx, the overall spatial clustering of the gene expression was nosier than in Xenium across all samples but in colorectal where the

distribution of Moran's I was more similar (**Figure 9c**). In order to determine whether the average levels of gene expression were capturing the biological transcripts, we compared the mean gene expression between *in situ* platforms and VISIUM CytAssist. For instance, in the case of the colorectal tumor sample, we can find a high correlation between these two modalities with no strong bias to the shared and unique genes of each panel (**Figure 9d**). However, there is a strong difference between lowly expressed genes in CosMx and Xenium. In the case of CosMx, we find an inflation within lowly expressed genes (mean UMIs < 0.1) that is indistinguishable from the average expression of control probes (horizontal dashed line in **Figure 9d**). The same patterns occur regardless of the sample we explore.

Next, we calculated the false discovery rate (FDR) for both platforms. Given the lack of ground truth, calculating the FDR can be challenging. For this reason, to account for the difference in panel size, we adjusted the FDR by the ratio between the gene panel size and the number of control probes (**Methods**). In this case, the FDR values for CosMx are two orders of magnitude higher than in Xenium (~10% compared to ~0.1%, respectively, **Figure 9e**). In the same line, the difference in counts between negative probes and gene probes was significantly higher in Xenium than in CosMx (fold of ~450 compared to ~3, respectively, **Figure 9f**).

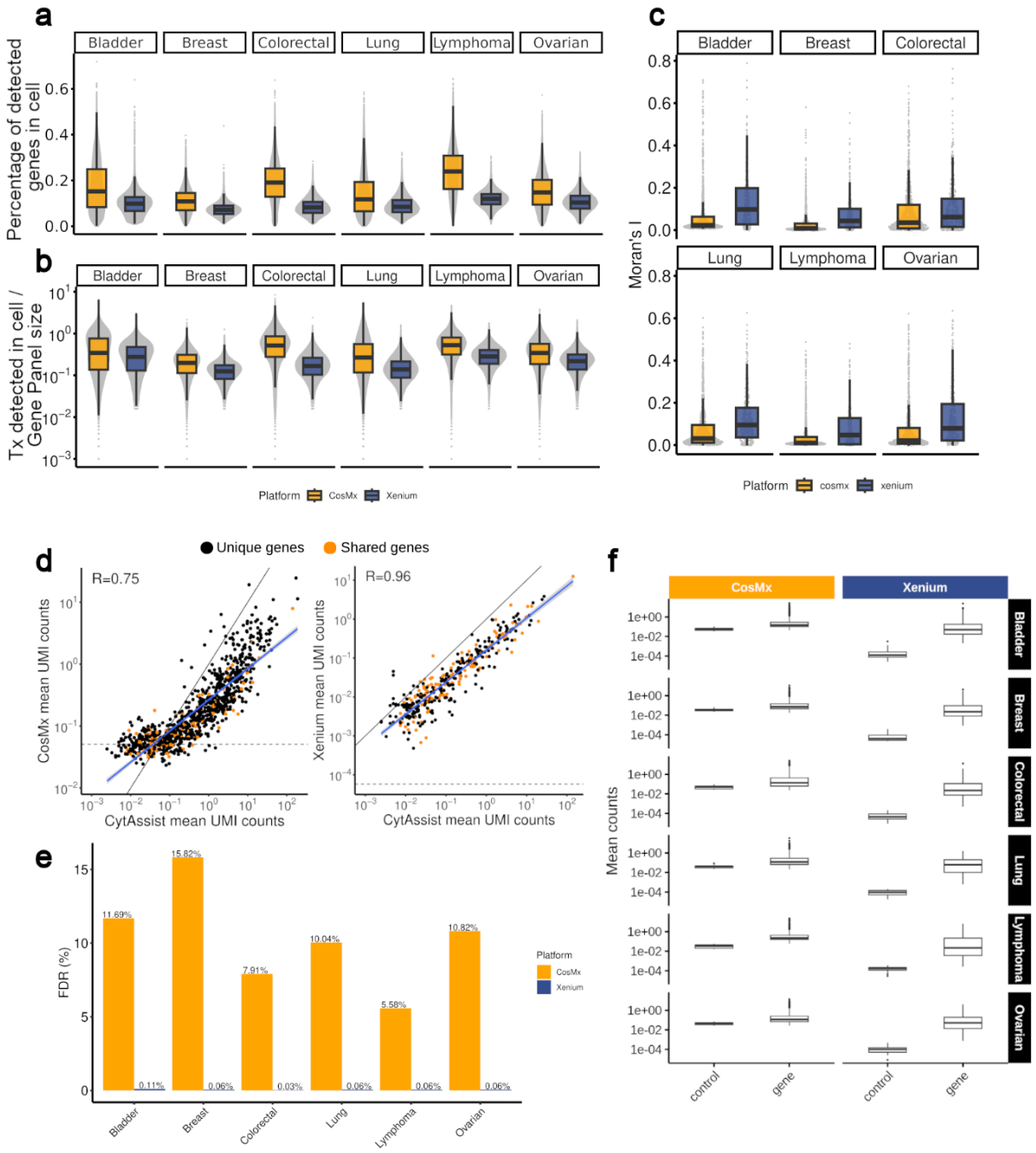

Figure 9 **– Transcript detection differences between in situ platforms. a)** Boxplot of the percentage of unique genes detected per cell in CosMx and Xenium. **b)** Boxplot of the number of transcripts detected per cell (y-axis, in log scale) in CosMx and Xenium after normalizing by the gene panel size (1000 and 377, respectively). **c)** Boxplot comparing the distribution of Morans'I in CosMx and Xenium samples. **d)** Scatterplots showing the correlation between mean gene expression in CytAssist and CosMx (left) or Xenium (right). The horizontal dashed lines show the average detection rate of the negative probes in Xenium and CosMx. The diagonal dashed line shows the expected perfect correlation (i.e x = y). The blue line shows the correlation between CosMx/Xenium and CytAssist. **e)** Barplot of the False Discovery Rate in CosMx and Xenium in each sample. **f)** Boxplots showing the mean expression of each negative control probe and each gene in CosMx and Xenium.

Finally, we explored the relationship between the quality of the RNA in the sample, measured as DV200, and the mean detected genes per cell (**Figure 10**). Overall, we observe a strong correlation between both variables in both platforms, suggesting that users should assess the RNA quality of their samples before proceeding to the experiment.

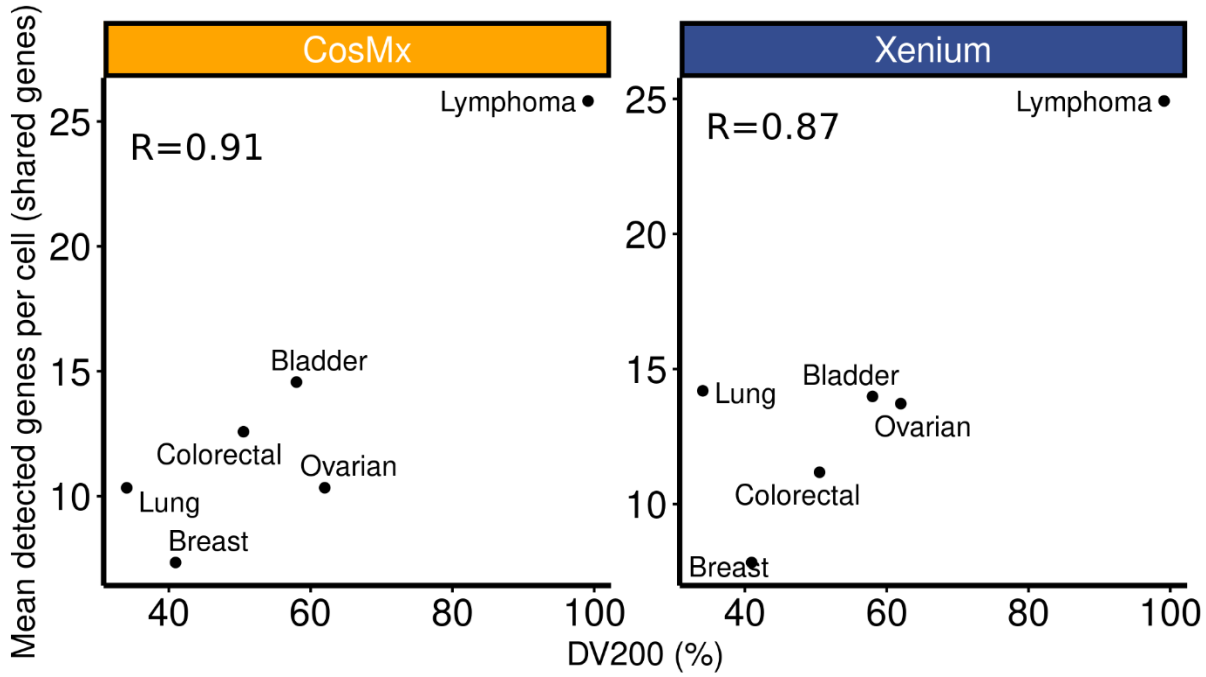

Figure 10 **– Impact of sample RNA quality and transcript detection. a)** Scatter plot representing the association between DV200 and the average number of genes detected per cell in CosMx (left) and Xenium (right), only overlapping genes are considered**.**

Then, we explored the transcript detection only considering the genes that overlap both panels. The average number of genes detected per cell is very similar (13.5 in CosMx and 14.3 in Xenium), with Xenium being slightly higher in bladder, lung, and ovarian and CosMx in colorectal (**Figure 11a**). In terms of transcripts counts per cell, however, Xenium gave a higher output (25.7 in CosMx and 37.3 in Xenium) in all samples (**Figure 11b**). Again, we used Moran's I as a proxy to assess the spatial clustering of the signal detected by each platform. The direct comparison of Moran's I showed higher random spatial patterns in CosMx gene expression in all samples (**Figure 11c**)**.** Almost 40% of the overlapped genes have a higher Moran's I in Xenium and very few genes higher in CosMx (**Figure 11d**). This difference in spatial arrangement can be seen mainly in immune genes. For instance, in the bladder sample we find *CD4* gene, a marker of CD4+ T cells which mediate anti-tumor activity[39], clustered expressed in one area in the Xenium while CosMx expressed this gene randomly across the whole tissue (**Figure 11e, top**). Same thing happens with *CTLA4*, an essential immune

checkpoint protein which is targeted in some immunotherapies[40] (**Figure 11e, bottom**). In this sense, CosMx could lead to wrong biological interpretation that could be critical if it is used for clinical aspects.

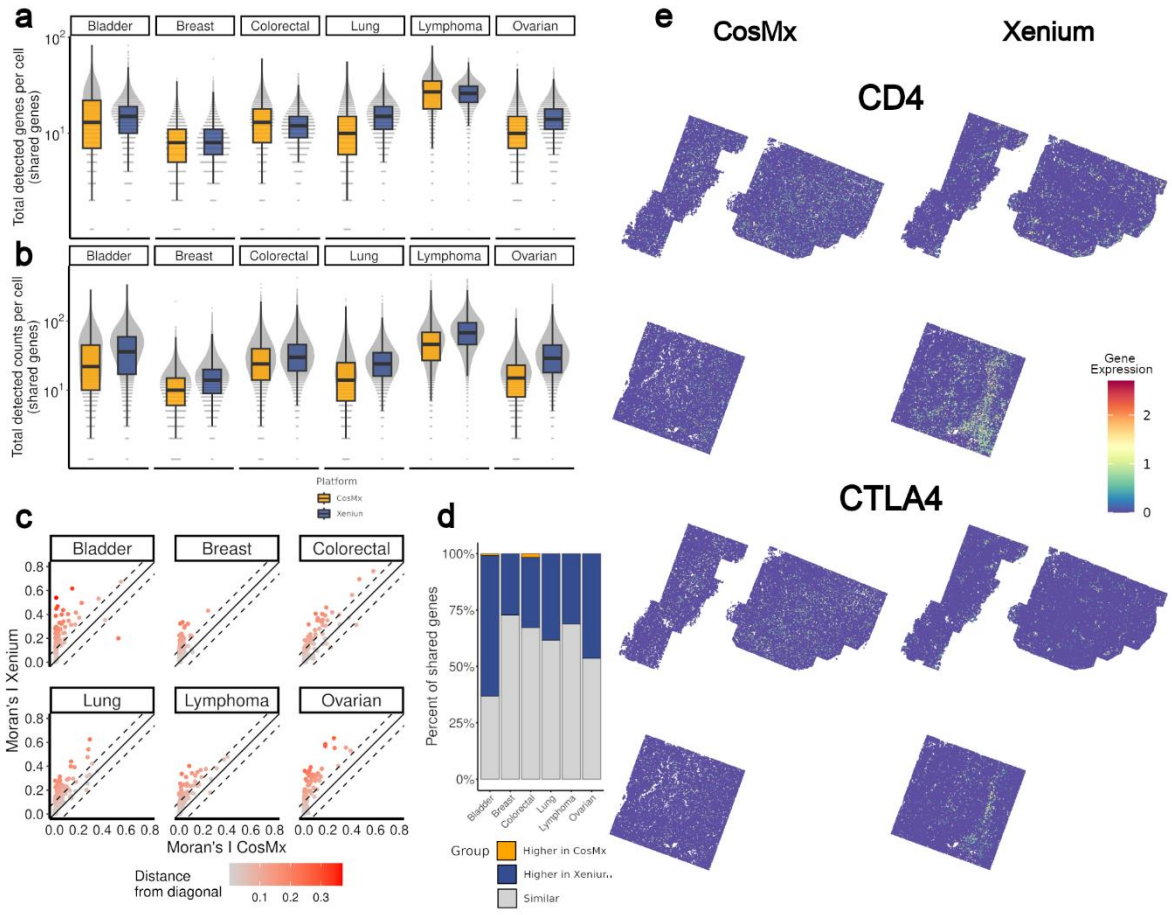

Figure 11 **– Comparison of in situ platforms after accounting for the main differences. a)** Boxplot of the number of unique genes detected per cell (y-axis, in log scale) in CosMx and Xenium considering only the 125 genes shared between the two gene panels. **b)** Boxplot of the number of transcripts detected per cell (y-axis, in log scale) in CosMx and Xenium considering only the 125 genes shared between the two gene panels. **c)** Scatter plot comparing the spatial distribution (Moran's I) of shared genes in CosMx and Xenium. The dots are colored according to the distance to the diagonal (equal Moran's I across platforms). **d)** Barplot showing the relative number of genes with similar spatial distribution or higher in one of the platforms in each sample. **e)** CD4 (top) and CTLA4 (bottom) gene expression in the CosMx (left) and Xenium(right) in the bladder sample.

5.3 Biological differences of *in situ* platforms

Given the differences in panel size, sensitivity, false discovery rate, and cell segmentation, we wondered to what extent both *in situ* platforms would yield similar insights into the biology of the samples. We first annotated all cells from both platforms with their estimated cell type based on their expression profile using SingleR[35]. Next, we re-assessed the same metrics as in the previous section but for each cell type. Overall, we observed similar patterns as when

analyzing the entire sample together. However, we found that cell area, number of unique genes and transcripts captured had specific patterns regarding the cell type. For example, cells residing in lower density regions such as smooth muscle and fibroblast had consistently higher cell size in Xenium, reflecting the impact of using nuclear expansion as cell segmentation strategy (**Figure 12a**). The only exception was T and NK cells in the lymphoma sample, which could be related to the higher differences of cells found and the lower overall cell size for Xenium. Regarding gene and transcript sensitivity, substantial differences were noted between platforms, particularly within immune cells. Notably, only cancer cells of epithelial origin demonstrated robust characterization, with no significant differences observed across these metrics.

Next, we assessed the differences in cell type composition of each sample inferred from each platform. Despite the differences in gene panel size, counts per gene, and cell size, the estimated cell composition in the shared area of both platforms is very similar in all samples, except the bladder sample, in which CosMx assigns more epithelial cells and fewer stromal and immune cells than Xenium (**Figure 12b**). Additionally, we noted notable differences in the assignment of monocytes and macrophages. While the total sum of these cell types remained consistent across platforms, CosMx allocated a smaller fraction to monocytes. Another aspect that caught our attention, though, is that the estimated cell fractions in a given sample using data from the same instrument can differ significantly depending on how much area of the sample one is studying. This can be seen in the Xenium data, for which we had two values: the cell fraction from the entire scanned area and that corresponding to the subset of the area shared with CosMx (**Figure 12b**). While in four samples these two values were relatively similar, in the other two (breast and colorectal), there were significant differences. Lastly, we explored their performance in identifying immune subtypes. In the lung and lymphoma samples, which contained a higher proportion of immune cells, we found that the distributions of B and T cell subtypes were nearly identical, except for memory and naive B cells, as well as effector and regulatory T cells **(Figure 12c).**

Despite their similar captured cell type composition, we investigated whether these cells exhibited comparable spatial distributions, given our previous finding that CosMx transcripts are noisier. For instance, if we focus on the lung epithelial cells across space, we find a similar spatial pattern that resembles the tissue morphology in both platforms (**Figure 12d, left**).

However, for CD8+ T cells, CosMx exhibits nosier patterns with a lack of clear spatial clustering compared to Xenium, even though both platforms showed enrichment of CD8+ T cells in the right area of the tissue (**Figure 12d, right**)**.** To quantify this observation, we used Moran's I metric, treating cell identity as binary data (**Figure 12e**). Xenium demonstrated higher spatial clustering of cell types, with notable differences in endothelial cells, CD4+ T cells, CD8+ T cells, monocytes, and memory B cells.

This phenomenon, the generation of biases in the estimated cell composition of a sample when studying only a small fraction of the tissue, is relatively intuitive and has been previously described in detail for other data modalities[27]. This is very important, as there is a tendency to limit spatial biology studies to relatively small sections of samples to optimize resources and the use of precious samples. Therefore, we decided to further understand and quantify the impact of the size of the scanned area when using *in situ* platforms. To that end, we simulated the estimated cell fraction if we had sampled with the Xenium different numbers of FOVs equivalent to the size of the CosMx instrument (0.5mm x 0.5mm). Then, we compared them to the actual value obtained with the full area, along with an additional control consisting of a random sampling of the same number of individual cells that can be found on average in a FOV but from any region of the tumor, simulating a single-cell experiment. As expected, there is a correlation between the number of FOVs analyzed and how closely the estimated cell composition resembles that of the entire tissue. For example, experiments sampling only one FOV, estimate the fraction of cancer cells anywhere between 5% and 55%, while the ground truth is 22% (**Figure 12f**). Notably, the variability in the simulated single-cell experiment was minimal and close to the ground truth, showing the relationship between spatial constraints and the amount of cells needed to quantify cell abundance.

Another important aspect is the limited size of the gene panel in Xenium can lead to missing important biology that goes beyond cell type classification. For instance, the *MMP7* gene, the expression of which is associated with invasive tumor growth, distant metastasis, and chemotherapy resistance in colorectal cancer, is absent in the Xenium gene panel. In our colorectal sample, overexpression of *MMP7* was observed in the cancer cells at the immediate edge with the stromal cells (**Figure 12g**), facilitating the identification of epithelial cell subpopulations with potential clinical relevance. These biological insights would be lost due to the small size of the Xenium panel. Finally, researchers must be aware of potential

biases that they might be introducing in their studies if they limit the amount of tissue being analyzed.

Overall, in the six samples we studied and with the panels and versions of the technology we have used, the raw data from Xenium seems to be, on average, of better quality than that of CosMx. These observations are consistent across most cell types present in our samples. That being said, CosMx data seemed to better capture the underlying biology for a subset of the genes. For example, the *ACTG2 expression*, which encodes the gamma (γ)-2 actin protein[41], should be primarily found in smooth muscle cells. However, we observed gene expression within epithelial cells in Xenium across all samples, contrasting with the specificity to non-epithelial cells seen in CosMx, which we validated in the CytAssist data (**Figure 12h**).

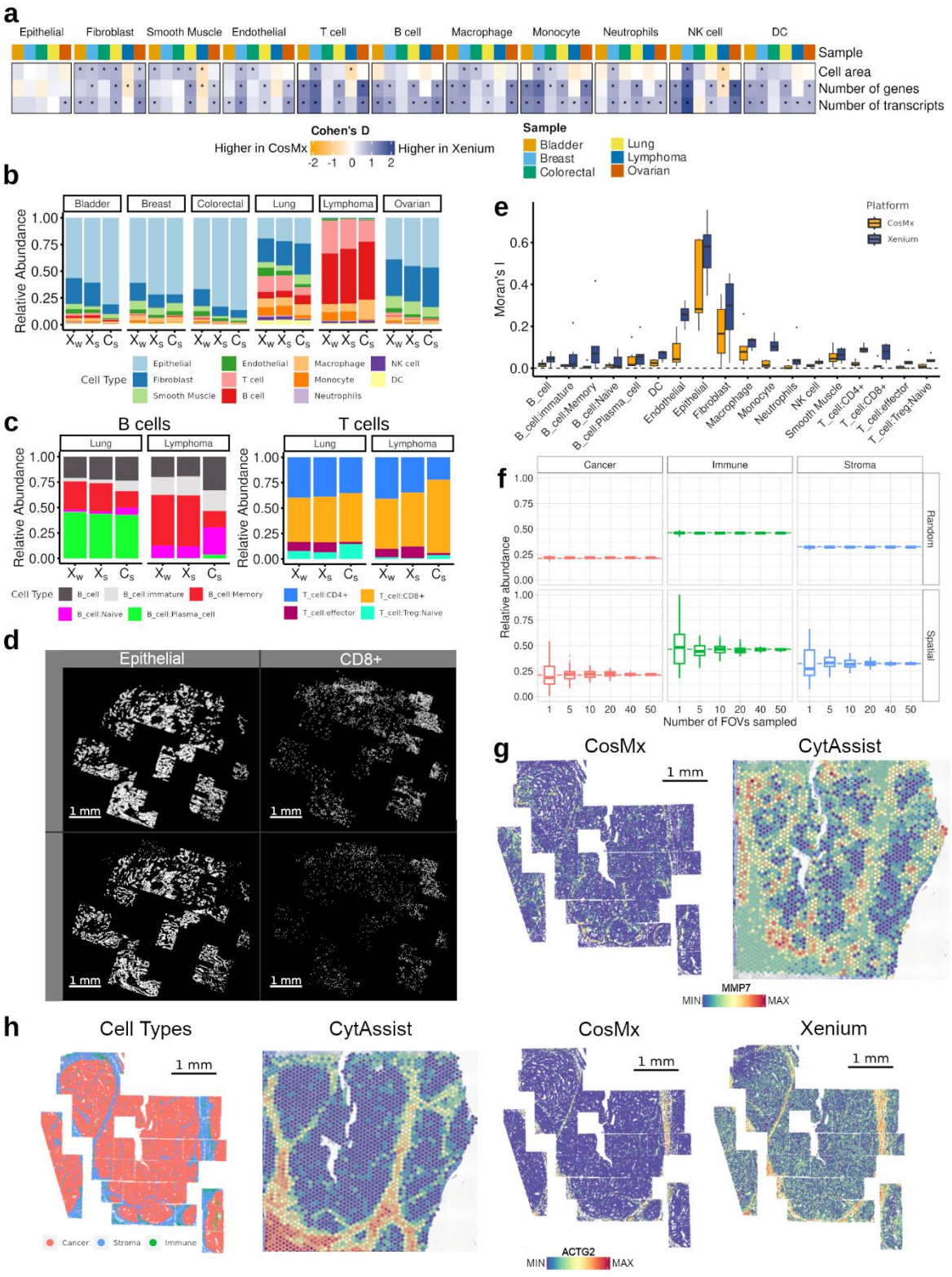

Figure 12 **– Identifying different cell types with each in situ platform. a)** Differences by cell type between Xenium and CosMx in cell size (top row), number of genes per cell (middle row), and number of transcripts per cell (bottom row), across all samples. Only the 125 genes shared between the two gene panels were considered. **b)** Barplot showing the cell type relative abundance found in the whole Xenium sample (left), the common area of the Xenium cells (middle) and the common area of the CosMx cells in each tumor sample. **c)** Similar to b) but showing the sub-type relative abundance within B cells (left) and T cells (right) for lung and lymphoma samples. **d)** Spatial distribution of epithelial cells (left) and CD8+ T cells (right) in a zoom area of the lung sample for

Xenium (top) and CosMx (bottom). **e)** Boxplot showing the global Moran's I computed in the binary data for each cell identity, sample and platform. **f)** Boxplot showing the effect of sampling smaller regions to compute relative abundance in the xenium Lung sample, of Cancer (epithelial), Stroma cells (fibroblast, smooth muscle and endothelial) and Immune (remaining cell types). In the Random category, the subset was determined by randomly sampling across the Xenium (shared area), while in the Spatial category, the sampling was based on FOV as a sampling unit. In each group number of sampled FOV, we used 100 stochastic iterations to compute the abundance of each cell group. Dashed lines represent the relative abundance of the Xenium (shared area) sample. **g)** MMP7 gene expression in the CosMx (left) and CytAssist (right) samples. **h)** Representation of the cancer, stromal and immune cells in the Xenium colon sample (first) and ACTG2 gene expression in the CytAssist (second), CosMx (third) and Xenium (fourth) samples.

5.4 Comparison of spatial transcriptomics and spatial proteomics

While RNA and protein levels for most genes tend to be highly correlated, this is not always the case. This is important, as oftentimes the molecular functions of any given gene are carried out not by its transcript, but by the protein it encodes. Therefore, in those cases where RNA and protein do not correlate, assessing the RNA to infer molecular function can be misleading. This includes important phenomena in cancer, such as disruption of protein-protein interactions by driver mutations, or lowering the levels of tumor suppressors by germline or somatic variants.

To assess to what extent spatial transcriptomics correlates with protein levels, we generated matching spatial proteomics data using the VISIUM CytAssist immuno-oncology panel, which includes 35 proteins. This panel can be generated during the regular VISIUM CytAssist protocol for spatial transcriptomics, and relies on antibodies tagged with a nucleotide sequence which are then labeled with the spatial barcode from the VISIUM spot.

In general terms, our five samples showed a weak correlation between gene and protein expression (**Figure 13a**) across all studied genes, with an average correlation coefficient around ~0.1. This is in stark contrast to the average correlation between RNA and protein levels for these genes in bulk data from the Clinical Proteogenomics Tumor Analysis Consortium (CPTAC)[36] across 7 cancer types (**Figure 13b**), where the average correlation coefficient is ~0.7.

When considering individual genes, we identified several distinct scenarios. First, positive correlations were observed between genes and proteins in cases where genes were sufficiently captured and exhibited a spatial distribution such as *ITGAX* in the lung sample (**Figure 13c, top**). Conversely, genes with correlations close to zero, predominantly cancer and

immune-related genes, tended to have low RNA expression, as illustrated by the example of *KRT5* in the lung sample (**Figure 13c, bottom**). Last, we encountered a third scenario where genes and proteins were both highly captured and had a similar spatial distribution but exhibited regions of overexpression. For instance, *CD68* showed a high gene expression uniquely in the upper-left part of the tissue adjacent to the adipose tissue (**Figure 13d**). While at the protein level, it also expressed an overlap in this area, but additionally showed high expression in the bottom-right area of the sample. Initially, we hypothesized that the differences between hotspots could be attributed to biological processes (i.e. mRNA translation or degradation) or the presence of distinct macrophage populations. However, we compared the gene expression of Xenium by creating pseudo spots after image registration of Xenium and CytAssist samples. Despite observing a slightly noisy spatial pattern, we found that regions with high expression of RNA (as inferred from Xenium) and protein were largely concordant, suggesting some differences in the quantification of the same gene by VISIUM and Xenium (**Figure 13e**). We explored whether this phenomenon extended to other genes, but our results show that, except for the bladder sample, this seems to be relatively rare (**Figure 13f**).

Overall, there are some intriguing and probably biologically relevant dynamics between the RNA and protein of several of the 35 genes we have studied. Such dynamics cannot be seen in bulk data, as evidenced by the CPTAC analysis. Instead, they can only be seen in spatial -omics platforms. Therefore, the future of the field must further the development of assays that allow the capture of multiple -omics readouts.

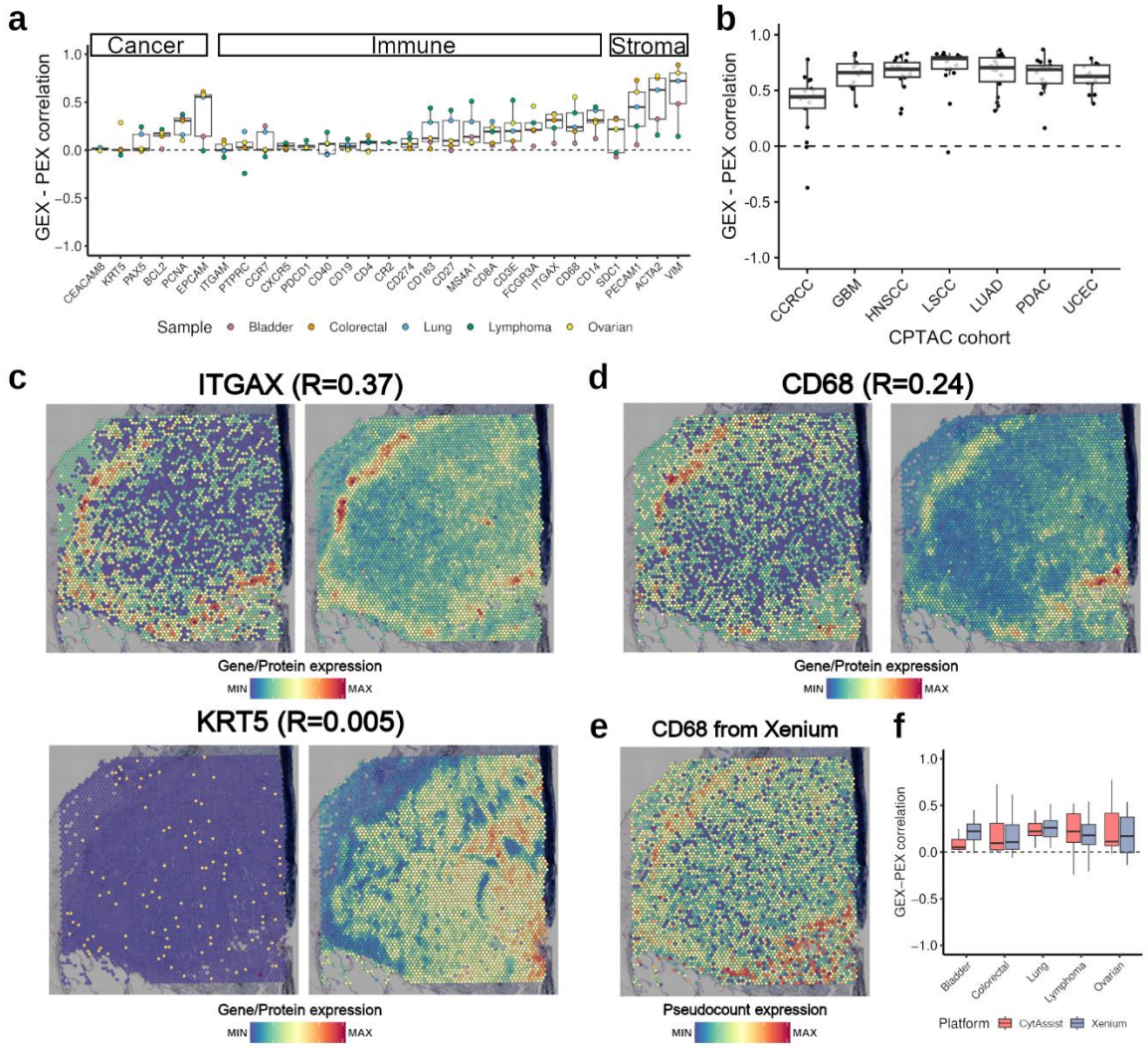

***Figure 13* – Spatial multi-omics reveals differences in RNA and protein levels across space. a)** Boxplots showing the correlation between normalized gene and protein expression in each sample represented by a color. Genes are sorted based on which cell type is expected to be overexpressed and their median correlation. **b)** Boxplot showing the correlation between RNA and protein for the 35 genes included in the CytAssist protein panel, according to the bulk measurements in 7 CPTAC cancer types. **c)** Normalized gene (left) and protein expression (right) of ITGAX (top) and KRT5 (bottom) in the Lung sample. Correlations between gene and protein expression are shown alongside gene symbols. **d)** Normalized gene (left) and protein expression (right) of ITGAX (top) in the Lung sample. Correlation between gene and protein expression are shown alongside gene symbol. **e)** Normalized gene expression of CD68 after transferring Xenium transcripts to CytAssist spots. **f)** Same as b) but correlations are computed using gene expression from CytAssist and the pseudo counts from Xenium. In both cases, only genes found in the protein and Xenium panel are considered.

6. Discussion

Spatial biology has revolutionized the understanding of key questions that are inherent in complex biological systems. One of the most promising applications is cancer research since it can provide an unprecedented understanding of the tumor microenvironment. This emerging field uses spatially resolved molecular profiling to map the intricate spatial relationships between cancer cells and their surrounding environment composed of immune

and stromal cells. By deciphering these complex spatial dynamics, researchers can gain critical insights into tumor heterogeneity, identify novel biomarkers and develop more effective targeted therapies.

Biological discoveries are associated with the development of new technologies or platforms that pursue to overcome the current limitations of the characterization of tumors. During the past years, a large span of platforms is available with their respective strengths and weaknesses to obtain the spatial landscape of tumors. For that reason, researchers who want to start in this field face the overwhelming barrier of which technology to use. To that end, here we have made a systematic comparison of four different spatial transcriptomics platforms when applied to FFPE human tumor samples from six cancer types. Furthermore, in as much as possible, we sectioned the samples for the different platforms on the same day to limit the impact of batch effects and maximize the comparability of the histological sections.

In terms of sequencing-based platforms, our results show most of the data is reproducible between CytAssist and VISIUM manual, there is significant improvement in overall data quality when using the CytAssist instrument. This is evidenced by the higher number of detected genes and transcripts in each spot as a better spatial architecture of the gene expression in the tissue. This can be attributed to both, better overall chemistry of the new version (with three probes per gene instead of one), as well as a potential improvement in analyte transfer that reduces the lateral diffusion of RNA molecules as we saw in the example of *ACTA2* in the colorectal sample. However, it is important to note the main limitation in both technologies is the resolution and the gap between spots that could mask the transcriptomic profile of the true biology in the tissue. A new sequencing-based platform, VISIUM-HD[42], will try to overcome this limitation by having a grid of continuous bins of 2 µm.

Regarding *in situ* platforms, our findings largely align with those previously described in the state-of-the-art section. In brief, we find a more accurate delineation of cell boundaries in CosMx despite being able to quantify the impact of transcript misassignment because we did not have a clear ground truth to compare. In the transcript detection, the quantity of transcripts captured in CosMx was higher compared to what the previous analysis reported. However, our results agreed with the nosier gene expression patterns that CosMx can be

influenced by the high FDR compared to Xenium. This could inflate the number of genes and transcripts found in CosMx cells. Nevertheless, when looking at cell typing, these differences in false discovery rate and segmentation do not seem to affect the overall results, as both platforms estimate similar cell fractions in most samples.

Another important aspect in our study is the quantification of the impact of amount of tissue area analyzed when establishing the cell type composition of a sample that was not explored in the previous studies. This is important since, to optimize precious clinical samples, many studies using spatial transcriptomics tend to analyze a relatively small area of each sample to, instead, increase the number of samples. One typical example is the use of TMAs, where one only studies a circle between 0.6mm and 1.2mm in diameter, which is significantly smaller than the capture area of VISIUM or the partial scan area of Xenium but allows fit more than one sample in each space, increasing the total number of analyzed samples. In line with previous studies working on spatial proteomics, we showed that reducing the analyzed area can lead to extremely biased cell composition estimates when considering spatial constraints. This has an important impact on CosMx as the user has to define the number of FOVs per run.

Finally, by using the VISIUM proteomics panel, we were able to compare the spatial distribution of transcripts and their corresponding proteins for the same tissue sample, revealing some very interesting dynamics. While considering the bulk relative abundance of gene and protein expression is correlated, we found that in the space only the majority of genes were not correlated. These were frequently caused by the lack of detection of RNA despite the presence of protein in the tissue. In other cases, the correlation between RNA and protein differed depending on the specific location within the sample, suggesting that the transcription / translation dynamics of these genes might differ. Given the significance of protein assays in clinical settings, especially the extensive use of immunohistochemistry in pathology labs for various diagnostic purposes, these findings highlight the crucial role of spatial multi-omics characterization of tumor samples.

As additional technologies for spatial transcriptomics become available, it will be essential to perform rigorous comparisons to help the community prioritize each of them based on their strengths, limitations, and the ultimate aims of the studies.

7. Limitations

This study must be considered in the context of the spatial transcriptomics field in late 2023. As mentioned, this field is growing and advancing at an extraordinary speed. Since then, improvements to the protocols have emerged for both products. Now it is available to order new gen panel covering 5000 genes in Xenium and 6000 in CosMx. Furthermore, CosMx is planning to release a whole transcriptome panel for the coming year. In terms of cell segmentation there are also new options available now, such their new multimodal cell segmentation kit which improves their weak point of inferring cell morphology using only nuclear staining. Even new technologies try to compete for achieving single-cell resolution and full coverage of the transcriptome like Curio Trekker[43] or VISIUM-HD[42].

In addition, we also have some limitations regarding the analysis of spatial platforms. We only analyzed data from the most used and commercially available platforms, not including many other spatial transcriptomics platforms. Moreover, we only covered six tumor types using patients and without any biological replicate. In the case of gene detection in *in situ* platforms, we had differences in gene panel size and a small fraction of genes shared across them (125). For a fairer comparison, the same number of genes and targets should be assessed for the effect of optical crowding. Finally, we did not have ground truth data from orthogonal approaches that could improve the assessment in the biological findings.

8. Future work

Since the spatial –omics field keeps evolving and new technologies appear, new benchmarks must be done reducing the external factors that can reduce the reliability of the comparison. We do not have plans for comparing the new gene panels, cell segmentation approaches, or different types of technologies. However, we are in the process of generating VISIUM-HD data from the consecutive sections of the samples used in this study. This new platform tries to converge the limitations of already available sequenced-based and *in situ* technologies by achieving single-cell resolution and whole transcriptome coverage. The results of this new data will complement the current study and provide meaningful insights to researchers that want to use spatial transcriptomics in their experiments.

9. References

1. Vandereyken, K., Sifrim, A., Thienpont, B. & Voet, T. Methods and applications for single-cell and spatial multi-omics. *Nat. Rev. Genet.* **24**, 494–515 (2023).
2. Miao, Z., Humphreys, B. D., McMahon, A. P. & Kim, J. Multi-omics integration in the age of million single-cell data. *Nat. Rev. Nephrol.* **17**, 710–724 (2021).
3. Lu, M. & Zhan, X. The crucial role of multiomic approach in cancer research and clinically relevant outcomes. *EPMA J.* **9**, 77–102 (2018).
4. Raufaste-Cazavieille, V., Santiago, R. & Droit, A. Multi-omics analysis: Paving the path toward achieving precision medicine in cancer treatment and immuno-oncology. *Front. Mol. Biosci.* **9**, 962743 (2022).
5. Ding, L. *et al.* Perspective on Oncogenic Processes at the End of the Beginning of Cancer Genomics. *Cell* **173**, 305-320.e10 (2018).
6. Supplitt, S., Karpinski, P., Sasiadek, M. & Laczmanska, I. Current Achievements and Applications of Transcriptomics in Personalized Cancer Medicine. *Int. J. Mol. Sci.* **22**, 1422 (2021).
7. Kwon, Y. W. *et al.* Application of Proteomics in Cancer: Recent Trends and Approaches for Biomarkers Discovery. *Front. Med.* **8**, 747333 (2021).
8. Schmidt, D. R. *et al.* Metabolomics in cancer research and emerging applications in clinical oncology. *CA. Cancer J. Clin.* **71**, 333–358 (2021).
9. Wang, H. *et al.* Development and application of transcriptomics technologies in plant science. *Crop Des.* **3**, 100057 (2024).
10. Li, X. & Wang, C.-Y. From bulk, single-cell to spatial RNA sequencing. *Int. J. Oral Sci.* **13**, 36 (2021).
11. Emrich, S. J., Barbazuk, W. B., Li, L. & Schnable, P. S. Gene discovery and annotation using LCM-454 transcriptome sequencing. *Genome Res.* **17**, 69–73 (2007).
12. Wang, Z., Gerstein, M. & Snyder, M. RNA-Seq: a revolutionary tool for transcriptomics. *Nat. Rev. Genet.* **10**, 57–63 (2009).
13. The Cancer Genome Atlas Research Network *et al.* The Cancer Genome Atlas Pan-Cancer analysis project. *Nat. Genet.* **45**, 1113–1120 (2013).
14. Haque, A., Engel, J., Teichmann, S. A. & Lönnberg, T. A practical guide to single-cell RNA-sequencing for biomedical research and clinical applications. *Genome Med.* **9**, 75 (2017).

15. Choi, J. R., Yong, K. W., Choi, J. Y. & Cowie, A. C. Single-Cell RNA Sequencing and Its Combination with Protein and DNA Analyses. *Cells* **9**, 1130 (2020).
16. Ståhl, P. L. *et al.* Visualization and analysis of gene expression in tissue sections by spatial transcriptomics. *Science* **353**, 78–82 (2016).
17. Lee, S., Kim, G., Lee, J., Lee, A. C. & Kwon, S. Mapping cancer biology in space: applications and perspectives on spatial omics for oncology. *Mol. Cancer* **23**, 26 (2024).
18. Moses, L. & Pachter, L. Museum of spatial transcriptomics. *Nat. Methods* **19**, 534–546 (2022).
19. Yue, L. *et al.* A guidebook of spatial transcriptomic technologies, data resources and analysis approaches. *Comput. Struct. Biotechnol. J.* **21**, 940–955 (2023).
20. Rodriques, S. G. *et al.* Slide-seq: A scalable technology for measuring genome-wide expression at high spatial resolution. *Science* **363**, 1463–1467 (2019).
21. Vickovic, S. *et al.* High-definition spatial transcriptomics for in situ tissue profiling. *Nat. Methods* **16**, 987–990 (2019).
22. Moffitt, J. R. & Zhuang, X. RNA Imaging with Multiplexed Error-Robust Fluorescence In Situ Hybridization (MERFISH). in *Methods in Enzymology* vol. 572 1–49 (Elsevier, 2016).
23. Eng, C.-H. L. *et al.* Transcriptome-scale super-resolved imaging in tissues by RNA seqFISH+. *Nature* **568**, 235–239 (2019).
24. Janesick, A. *et al.* High resolution mapping of the tumor microenvironment using integrated single-cell, spatial and in situ analysis. *Nat. Commun.* **14**, 8353 (2023).
25. He, S. *et al.* High-plex imaging of RNA and proteins at subcellular resolution in fixed tissue by spatial molecular imaging. *Nat. Biotechnol.* **40**, 1794–1806 (2022).
26. Spatial Gene Expression - 10x Genomics. https://www.10xgenomics.com/products/spatial-gene-expression.
27. CosMx™ SMI vs. Xenium: Comparative Analysis of Breast Tissue | NanoString. https://nanostring.com/resources/cosmx-smi-vs-xenium-comparative-analysis-of-breast-tissue/?utm_source=google&utm_medium=paidsearch&utm_campaign=dynamic&utm_id=NSTG_DynamicSearch&utm_source=google&utm_medium=cpc&utm_campaign=1765548394&utm_agid=132844584422&utm_term=&creative=618340999371&device=c&placement=&network=g&gad_source=1&gclid=CjwKCAjwvIWzBhAlEiwAHHWgvUf-_cRuDGX5CzcZmm7eynTd7cMMtd-DV6Hi6mUQLlu5VS_umN9OChoC3LEQAvD_BwE.

28. Wang, H. *et al.* Systematic benchmarking of imaging spatial transcriptomics platforms in FFPE tissues. Preprint at https://doi.org/10.1101/2023.12.07.570603 (2023).
29. Cook, D. P. *et al.* A Comparative Analysis of Imaging-Based Spatial Transcriptomics Platforms. Preprint at https://doi.org/10.1101/2023.12.13.571385 (2023).
30. Hartman, A. & Satija, R. Comparative analysis of multiplexed in situ gene expression profiling technologies. Preprint at https://doi.org/10.1101/2024.01.11.575135 (2024).
31. Sibai, M. *et al.* The spatial landscape of Cancer Hallmarks reveals patterns of tumor ecology. Preprint at https://doi.org/10.1101/2022.06.18.496114 (2022).
32. Hao, Y. *et al.* Dictionary learning for integrative, multimodal and scalable single-cell analysis. *Nat. Biotechnol.* **42**, 293–304 (2024).
33. Manukyan, A. *et al.* VoltRon: A Spatial Omics Analysis Platform for Multi-Resolution and Multi-omics Integration using Image Registration. Preprint at https://doi.org/10.1101/2023.12.15.571667 (2023).
34. Larsson, L., Franzén, L., Ståhl, P. L. & Lundeberg, J. *Semla:* a versatile toolkit for spatially resolved transcriptomics analysis and visualization. *Bioinformatics* **39**, btad626 (2023).
35. Aran, D. *et al.* Reference-based analysis of lung single-cell sequencing reveals a transitional profibrotic macrophage. *Nat. Immunol.* **20**, 163–172 (2019).
36. Liang, W.-W. *et al.* Integrative multi-omic cancer profiling reveals DNA methylation patterns associated with therapeutic vulnerability and cell-of-origin. *Cancer Cell* **41**, 1567-1585.e7 (2023).
37. Fakatava, N. *et al.* Actin alpha 2, smooth muscle, a transforming growth factor-β1-induced factor, regulates collagen production in human periodontal ligament cells via Smad2/3 pathway. *J. Dent. Sci.* **18**, 567–576 (2023).
38. Sahin, F. E. & Tanguay, A. R. Distortion optimization for wide-angle computational cameras. *Opt. Express* **26**, 5478 (2018).
39. Speiser, D. E., Chijioke, O., Schaeuble, K. & Münz, C. CD4+ T cells in cancer. *Nat. Cancer* **4**, 317–329 (2023).
40. Sobhani, N. *et al.* CTLA-4 in Regulatory T Cells for Cancer Immunotherapy. *Cancers* **13**, 1440 (2021).
41. Edfeldt, K., Hellman, P., Westin, G. & Stalberg, P. A plausible role for actin gamma smooth muscle 2 (ACTG2) in small intestinal neuroendocrine tumorigenesis. *BMC Endocr. Disord.* **16**, 19 (2016).
42. Visium HD Spatial Gene Expression - 10x Genomics. https://www.10xgenomics.com/products/visium-hd-spatial-gene-expression.

43.Convert single-cell omic into spatial data | Curio Trekker. https://curiobioscience.com/curio-trekker/.

10. Appendix

Manuscript Online Version

The manuscript summarizing the results obtained in this master thesis can be found at bioRxiv (https://doi.org/10.1101/2024.05.21.593407)

Code Reproducibility

Scripts used in this master thesis can be found at https://github.com/scervilla/TFM_benchmark